

1 **Aqueous OH-initiated photooxidation of smoke extracts from maize**
2 **straw and coal combustion: optical character and molecular**
3 **composition**

4 Zhaolian Ye¹, Dandan Hu¹, Qiuyan Chen¹, Xiangpeng Huang¹, Xinlei Ge²

5 ¹ School of Resources and Environmental Engineering, Jiangsu University of
6 Technology, Changzhou 213001, China

7 ² School of Energy and Environment, Southeast University, Nanjing, 211189, China.

8 Correspondence: Zhaolian Ye (bess_ye@jsut.edu.cn) and Xinlei Ge
9 (xinlei@seu.edu.cn)

10 **Abstract:** Aqueous-phase •OH photodegradation of coal- and maize-derived smoke
11 extracts was investigated to elucidate their optical and molecular transformations.
12 Parallel factor analysis of excitation-emission matrix fluorescence spectra identified
13 one humic-like and two protein-like substances. FT-ICR MS revealed that CHO (74.5%
14 for maize, 58.9% for coal) and CHON (24.1% for maize, 11.8% for coal) compounds
15 dominated both smoke extracts, whereas sulfur-containing species were more abundant
16 in coal smoke (29.4%) than in maize (1.4%). The aqueous •OH photooxidation
17 enhanced molecular saturation and reduced aromaticity, reflected by lower double bond
18 equivalent and aromaticity index values. The abundance of lignin-like compounds
19 decreased, whereas lipid- and aliphatic-like fractions increased, suggesting a
20 transformation of aromatic species into more saturated products, which
21 correspondingly reduced light absorption and overall fluorescence intensity. Distinct
22 photodegradation pathways were observed for coal and maize extracts based on
23 changes in resistant, degraded, and newly formed molecules. Reactive species

24 contributed to WSOC degradation in the order $\bullet\text{OH} > {}^3\text{C} > {}^1\text{O}_2$, with contributions of
25 86.4%, 12.8%, and 0.8% for coal extracts, and 80.9%, 16.0%, and 3.1% for maize
26 extracts, respectively. Increased oxalic acids, CHO_2^+ fragments, and declining pH
27 values during the first 5 h indicated substantial formation of carboxylic acids.
28 Measurements from aerosol mass spectrometry showed increasing oxidation indicators
29 during this early stage, confirming enhanced oxidation of aqueous secondary organic
30 aerosol. Oxidative potential, assessed by dithiothreitol consumption, initially increased
31 and then declined, while its normalization by water-soluble organic carbon increased,
32 likely due to the formation of nitrogen-containing compounds in coal smoke and
33 reactive quinones in maize smoke, respectively. Overall, this study improves
34 understanding of aqueous-phase photochemical processing of smoke-derived water-
35 soluble organic matter and supports more accurate representation of these processes in
36 atmospheric models, contributing to better assessments of smoke aging impacts on air
37 quality and climate.

38 **Keywords:** molecular transformations, optical characteristic, FT-ICR MS, reactive
39 species, dithiothreitol (DTT) consumption rate

40

41 **1 Introduction**

42 The atmospheric aqueous phase contains a variety of oxidants, such as hydrogen
43 radical ($\bullet\text{OH}$), peroxy radicals, singlet oxygen (${}^1\text{O}_2$), and excited triplet states of
44 organic compounds (${}^3\text{C}^*$), which can trigger aqueous-phase oxidation reaction.
45 Aqueous-phase process has been recognized as a significant source of secondary
46 organic aerosol (SOA) and key contributors to light-absorbing compounds, thereby

47 influencing radiative forcing and air quality (Arciva et al., 2024; Go et al., 2023).
48 Extensive studies have investigated the chemical composition, light-absorption
49 properties, and SOA mass yield from single-component model compounds (Arciva et
50 al., 2022; Li et al., 2022). Recently, increasing attention has been toward the aqueous
51 photoaging of complex mixtures, including laboratory-generated SOA or
52 multicomponent systems (Gerritz et al., 2024; Go et al., 2024). Moreover, studies on
53 aqueous aging of water-soluble organic matter (WSOM) derived from actual smoke
54 particle or PM_{2.5} extracts provide valuable insights into aqueous-phase processing
55 under more realistic atmospheric conditions (Fan et al., 2018; Hems et al., 2020; Wong
56 et al., 2017). Organic matter (OM) within smoke particles, which accounts for up to 60-
57 90% of total mass, is a complex mixture of aromatic and aliphatic compounds with
58 diverse functional groups. The chemical complexity of these precursors poses
59 challenges for comprehensive product characterization and mechanistic studies.
60 Molecular-level compositional data are therefore crucial for improving our
61 understanding of the role of smoke-derived OM in atmospheric aqueous-phase
62 chemistry. High-resolution mass spectrometry (MS) techniques with soft ionization
63 methods, such as Fourier transform ion cyclotron resonance mass spectrometry (FT-
64 ICR MS), enable detailed molecular characterization in complex mixtures and have
65 been widely applied in aerosol studies (Cao et al., 2025; Wang et al., 2017).

66 To date, only a few studies (Leresche et al., 2021; Lei et al., 2024) have examined
67 photochemical aging characteristics of aqueous extracts of smoke particles or
68 atmospheric fine particulate matter, most of which have appeared only recently. Notably,
69 few investigations have compared the molecular and optical changes during aqueous-
70 phase oxidation of smoke extracts from different fuel sources. Cao et al. (2025)
71 compared molecular-level composition and fluorophore changes of extracted WSOM,

72 but their study did not consider the distinct contributions of various reactive oxygen
73 species (ROS) to the oxidation process. Additionally, the wavelength of the light source
74 can significantly influence the photochemical reactivity of organic compounds. For
75 instance, syringaldehyde was found to inhibit the degradation of vanillyl alcohol under
76 UV-B irradiation due to light-absorbing competition, whereas it promoted the
77 degradation of vanillyl alcohol under UV-A irradiation via the photosensitization effect
78 of syringaldehyde (Li et al., 2024).

79 To elucidate the reaction mechanism involved in aqueous-phase photooxidation,
80 it is crucial to understand the formation, transformation, and roles of ROS during
81 photolysis. Biomass burning smoke—such as that produced from agricultural crop
82 residues—contains a variety of potential organic photosensitizers bearing with carbonyl
83 groups and conjugated double bonds, which can absorb sunlight and generate ROS (e.g.,
84 HO_2/O_2^- , $^1\text{O}_2$, $\bullet\text{OH}$), thereby enhancing atmospheric oxidative capacity. However,
85 direct quantification of ROS remains challenging (Gerritz et al., 2024; Leresche et al.,
86 2021; Manfrin et al., 2019). For instance, Gerritz et al. (2024) investigated the
87 photolytic formation of ROS in aqueous extracts of laboratory-generated SOA using an
88 in situ UV-vis irradiation system coupled with electron paramagnetic resonance (EPR)
89 spectroscopy and identified organic peroxides and carbonyls as major ROS precursors.
90 Manfrin et al. (2019) reported the $^1\text{O}_2$ formation from photosensitized reactions
91 mediated by aromatic SOA, although free radicals were not directly measured. Due to
92 the chemical complexity of smoke-derived WSOM and the analytical difficulty in
93 quantifying ROS, the underlying reaction mechanisms remain poorly understand.

94 Further investigation into the aqueous photoaging of WSOM from different
95 combustion sources is crucial to understanding the underlying mechanisms driving

96 chemical transformation and light absorption. Comparative studies of maize- and coal-
97 derived WSOM under simulated sunlight can reveal how source-dependent
98 compositions influence photo-reactivity and light-absorbing compounds formation.
99 This study compares the optical, molecular evolution and oxidative potential of maize
100 (a representative agricultural residue) and coal smoke extracts during OH-induced
101 photooxidation. WSOM from both smoke types were analyzed using UV-vis
102 spectrometer, excitation-emission matrix (EEM) fluorescence, and FT-ICR MS to
103 identify similarities and differences in photoaging behavior. High-resolution time-of-
104 flight aerosol mass spectrometers (HR-AMS) were used to characterize the bulk
105 chemical composition of low-volatility organics (denoted as aqSOA) over
106 photoreaction. Our findings will provide insights into the chemical evolution and
107 environmental impacts of smoke-derived organic matter.

108

109 **2 Materials and Methods**

110 **2.1 Chemicals and solutions**

111 The following reagents were purchased from the Sigma-Aldrich
112 (dithiothreitol, >99%; 5,5'-dithiobis (2-nitrobenzoic acid), >99%; benzoic acid, >99%;
113 syringol, >99%; furfuryl alcohol, >99%). Methanol ($\geq 99\%$), acetonitrile ($\geq 99\%$),
114 Na_2CO_3 ($\geq 99\%$) and NaHCO_3 ($\geq 99\%$) were purchased from Acros Chemicals.
115 Sulfuric acid ($\geq 99\%$) was obtained from Sinopharm. $(\text{NH}_4)_2\text{SO}_4$ (GR), H_2O_2
116 (29%~32%) and KOH ($\geq 99\%$) were supplied by Aladdin and Alfa Aesar, respectively.
117 2,2,6,6-Tetramethylpiperidine ($\geq 98\%$) and 5,5-dimethyl-1-pyrroline N-oxide ($\geq 97\%$)
118 were purchased from Anpel Laboratory Technologies (Shanghai) Co., Ltd.

119 All chemicals were used as received without further purification. All solutions
120 were prepared with ultrapure water (resistivity \geq 18.2 M Ω cm) produced by a Milli-Q
121 purification system.

122 **2.2 Sample collection and experiment preparation**

123 Coal and maize straw were collected from Lingwu (Ningxia) and Shangqiu (Henan
124 Province), respectively, and combusted in a self-built stove designed to simulate
125 domestic fuel burning conditions. Smoke particle collection followed the procedures
126 described in our previous study (Ye et al., 2025). Briefly, the stove was connected to a
127 stainless steel dilution tunnel and residence chamber. Smoke particles emitted from
128 maize straw and coal combustion were collected on pre-baked quartz fiber filters (20.3
129 \times 25.4 cm, Whatman) using two samplers equipped with cyclone with a 2.5 μ m
130 aerodynamic cutoff.

131 One quarter of each filter was cut into strips and placed in extraction bottles. The
132 samples were ultrasonically extracted three times with 30 mL Milli-Q water. The
133 combined extracts were filtered through a 0.45 μ m PTFE membrane and subsequently
134 diluted to approximately 15 mgC/L for photoaging experiment based on suggested TOC
135 level (0.5-1.4 mmol C/L) by Cook et al. (2017) for cloud water. Photochemical
136 reactions were performed in a Rayonet RPR-200 photoreactor equipped with 14 lamps,
137 following the procedure described in our previous study (Ye et al., 2025). The irradiance
138 intensity on the solution surface was 2.4 mW/cm² in the wavelength region of 290-400
139 nm (centered at 313 nm), as measured by a radiometer (Photoelectric Instrument
140 Factory of Everfine Corporation, Hangzhou, China). The intensity is slight lower than

141 natural sunlight levels (6.16 mW/cm²) measured at noon during winter at Jiangsu
142 University of Technology (Wang et al., 2025). Before photooxidation, 10 mM H₂O₂
143 was added to the reaction solution to generate •OH with certain concentration,
144 consistent with previous study (Arciva et al., 2022; Cao et al., 2025).

145 **2.3 Chemical analysis**

146 Water-soluble organic carbon (WSOC) concentrations were determined using a
147 total organic carbon (TOC) analyzer (TOC-L CPH, Shimadzu, Japan). Metal element
148 concentrations (Fe and Cu) were quantified by inductively coupled plasma-mass
149 spectrometry (ICP-MS, Agilent 7800). Eight water soluble inorganic ions (Na⁺, Cl⁻,
150 SO₄²⁻, NO₃⁻, K⁺, NH₄⁺, Ca²⁺ and Mg²⁺) were also detected for both smoke extracts.
151 Details can be found in Sect. S1 in the Supplement. These detection limits were
152 determined based on three times the standard deviation of blank sample. The method
153 detection limits ranged from 5-20 µg/L for anions and 0.5-2 µg/L for cations. The
154 detection limits of Fe and Cu are 2.0 µg/L and 0.8 µg/L, respectively.

155 **2.4 UV-vis and EEM analysis**

156 The UV-vis absorption spectra were monitored using UV-vis spectrophotometer
157 (Shimadzu, Japan) over wavelength range of 200-700 nm. The mass absorption
158 coefficients (MACs, m²/gC), defined as absorbance normalized by WSOC
159 concentration, were calculated as follows:

$$160 \quad MAC_{\lambda} = \frac{A_{\lambda}}{C \times L} \times \ln 10 \quad (1)$$

161 Where A_{λ} represent the absorbance at wavelength λ . C refers to the WSOC
162 concentration of reaction solution. L is the optical path length (1 cm in this study).

163 The EEM spectra were recorded using a three-dimensional fluorescence

164 spectrophotometer (FluoroMax Plus, HORIBA Scientific). Parallel factor analysis
165 (PARAFAC) model was applied to EEM spectra to resolve the fluorescent compounds
166 using the DOMFluor toolbox in MATLAB 2021b. Details of the determination and
167 modeling procedures are provided in our previous study (Ye et al., 2025). Three
168 fluorescence components (C1, C2 and C3) were identified from PARAFAC model. The
169 fluorescence index (FI), humification index (HIX), and biological index (BIX) were
170 further calculated to characterize the fluorescent properties of the samples. The
171 calculation methods for these indicators were shown in the supplement and in our
172 previous study (Ye et al., 2025).

173 **2.5 FT-ICR MS measurement**

174 The molecular compositions, degree of unsaturation, and aromaticity of WSOM
175 were characterized using FT-ICR MS coupled with negative electrospray ionization
176 (ESI-). Solid-phase extraction (SPE) was employed for sample pretreatment prior to
177 FT-ICR MS determination, following procedures similar to those described in previous
178 studies (Yang et al., 2025). Briefly, the reaction solution was adjusted to pH 2 and pass
179 through SPE cartridges (Oasis HLB, Waters, USA) preconditioned with 15 mL
180 methanol and 10 mL Milli-Q water. The retained organic matter was subsequently
181 eluted with 10 mL methanol. The eluate was then concentrated to approximately 0.5
182 mL using a rotary evaporator and stored at -20 °C until analysis. Prior to analysis, the
183 sample was re-dissolved in 4 mL of methanol and filtered through a 0.22 µm PTFE
184 membrane. FR-ICR MS analysis was performed with a capillary voltage of 4.0 kV, and
185 samples were introduced into the ESI source at a flow rate of 120 µL/ h. Mass spectra
186 were acquired over the m/z range of 150–800 Da. To improve the signal-to-noise ratio
187 and dynamic range, each spectrum was averaged from 200 scans. Blank samples were

188 analyzed under the same procedure. Notably, no water-insoluble precipitates larger than
189 0.22 μm were observed during photooxidation. However, filtration of the reaction
190 solution through a 0.22 μm membrane prior to analysis may result in the loss of some
191 newly formed oligomers.

192 The Composer software (Sierra Analytics, USA) was utilized to process the FT-ICR
193 MS spectra and assign elemental compositions to recalibrated peaks, with a mass
194 tolerance of ± 1.0 ppm and a signal-to-noise ratio (S/N) threshold of ≥ 4 . Based on the
195 assigned molecular formulas, WSOM compounds were categorized into four groups:
196 CHO, CHON, CHOS, and CHONS. To evaluate the degree of unsaturation and
197 aromaticity, double bond equivalent (DBE) and aromaticity index (AI) were calculated
198 as follows:

$$199 \quad \text{DBE} = \frac{1}{2} \times (2c + 2 - h + n) \quad (2)$$

$$200 \quad \text{AI} = \frac{1 + c - 0.5o - s - 0.5h}{c - 0.5o - s - n} \quad (3)$$

201 The intensity-weighted averaged characteristic parameters can be expressed as:

$$202 \quad P_w = (\sum P_i \times I_i) / \sum I_i \quad (4)$$

203 where P represents DBE, AI, molecular weight (MW), oxygen-to-carbon (O/C) or
204 hydrogen-to-carbon (H/C) ratio. P_i represents the corresponding parameter value for
205 each individual compound I , and I_i represents the relative abundance of its molecular
206 formula.

207 Molecular formulas were further classified into seven compound classes based on
208 their H/C and O/C ratios (Ning et al., 2025): lipid-like ($1.5 < \text{H/C} \leq 2.0$, $0 \leq \text{O/C} \leq 0.3$);
209 aliphatic -like ($1.5 < \text{H/C} \leq 2.2$, $0.3 < \text{O/C} \leq 0.67$); lignin-like ($0.67 < \text{H/C} \leq 1.5$, $0.1 \leq$

210 O/C < 0.67); carbohydrate-like ($1.5 < H/C \leq 2.5$, $0.67 < O/C < 1.2$); unsaturated
 211 hydrocarbon-like ($0.67 < H/C \leq 1.5$, $O/C < 0.1$); unsaturated aromatic-like ($0.2 \leq H/C \leq$
 212 0.67 , $O/C < 0.67$), and tannin- ($0.6 < H/C \leq 1.5$, $0.67 \leq O/C \leq 1.2$). The saturated
 213 compounds were defined as the sum of lipid-like and aliphatic components.

214 2.6 High-resolution mass spectrometry analysis

215 High-resolution aerosol mass spectrometer (HR-AMS, Aerodyne Res. Inc.) was used
 216 to characterize the bulk chemical composition of aqSOA, including average elemental
 217 ratios (i.e., oxygen-to-carbon ratio (O/C) and hydrogen-to-carbon ratio (H/C)) and
 218 some specific fragment ions. The average oxidation state of carbon ($O_{Sc} = 2 \times$
 219 $O/C - H/C$) was used to index the oxidation degree of aqSOA. 10 mg/L ammonium
 220 sulfate was added into the solution as an internal standard for quantifying SOA mass
 221 concentration. The aqSOA mass yield was calculated as follows:

222

$$223 \quad \text{aqSOA yield} = \frac{[Org]_t - [Org]_0}{[WSOC]_0 - [WSOC]_t} = \frac{[Org]_t \times \frac{[SO_4^{2-}]_t}{[SO_4^{2-}]_{AMS,t}} - [Org]_0 \times \frac{[SO_4^{2-}]_0}{[SO_4^{2-}]_{AMS,0}}}{([WSOC]_0 - [WSOC]_t) \times M/12}$$

224 (5)
225

226 Where $[SO_4^{2-}]_t$ and $[SO_4^{2-}]_0$ denote sulfate concentrations (mg/L) in the solution at
 227 irradiation time t and zero, respectively. Here, $[SO_4^{2-}]_t$ was equal to $[SO_4^{2-}]_0$ assuming
 228 sulfate was not loss during irradiation. The $[Org]$ and $[SO_4^{2-}]_{AMS}$ denote the apparent
 229 concentrations of aqSOA and sulfate measured by HR-AMS. $[WSOC]_t$ and $[WSOC]_0$
 230 were WSOC concentrations in the solution measured by TOC at irradiation time t and
 231 zero, respectively. M represents the averaged molecular weight of mixed solution
 232 which can be estimated by FT-ICR MS.

233 **2.7 ROS determination based on electron paramagnetic resonance**

234 Electron paramagnetic resonance (EPR) spectroscopy (Bruker EMXnano, Germany)
235 was used to detect ROS. 5,5-Dimethyl-1-pyrroline N-oxide (DMPO) and 2,2,6,6-
236 tetramethylpiperidine (TEMP) were used as spin-trapping agents for $\bullet\text{OH}$ and $^1\text{O}_2$ to
237 identify the DMPO-OH adducts (1:2:2:1) and the TEMPO adducts (1:1:1), respectively
238 (Hu et al., 2025; Wang et al, 2020). The 10 mL of aqueous extracts were diluted into
239 100 mL using deionized water and pH was adjusted at 5.0 ± 0.1 with 0.1 M H_2SO_4
240 solutions. Then 100 mM of two spin-trapping agents were added into the 50 mL of
241 acidified aerosol extract solutions. After photodegradation of smoke extracts, 200 μL
242 of solutions were transferred from the reaction solutions and immediately analyzed by
243 EPR. The EPR parameters were set as following: modulation frequency of 100 kHz;
244 center field of 3460 G, modulation amplitude of 1G, microwave power of 25 mW,
245 sweep width of 200 G, sweep time of 150 s, number of scans of 20.

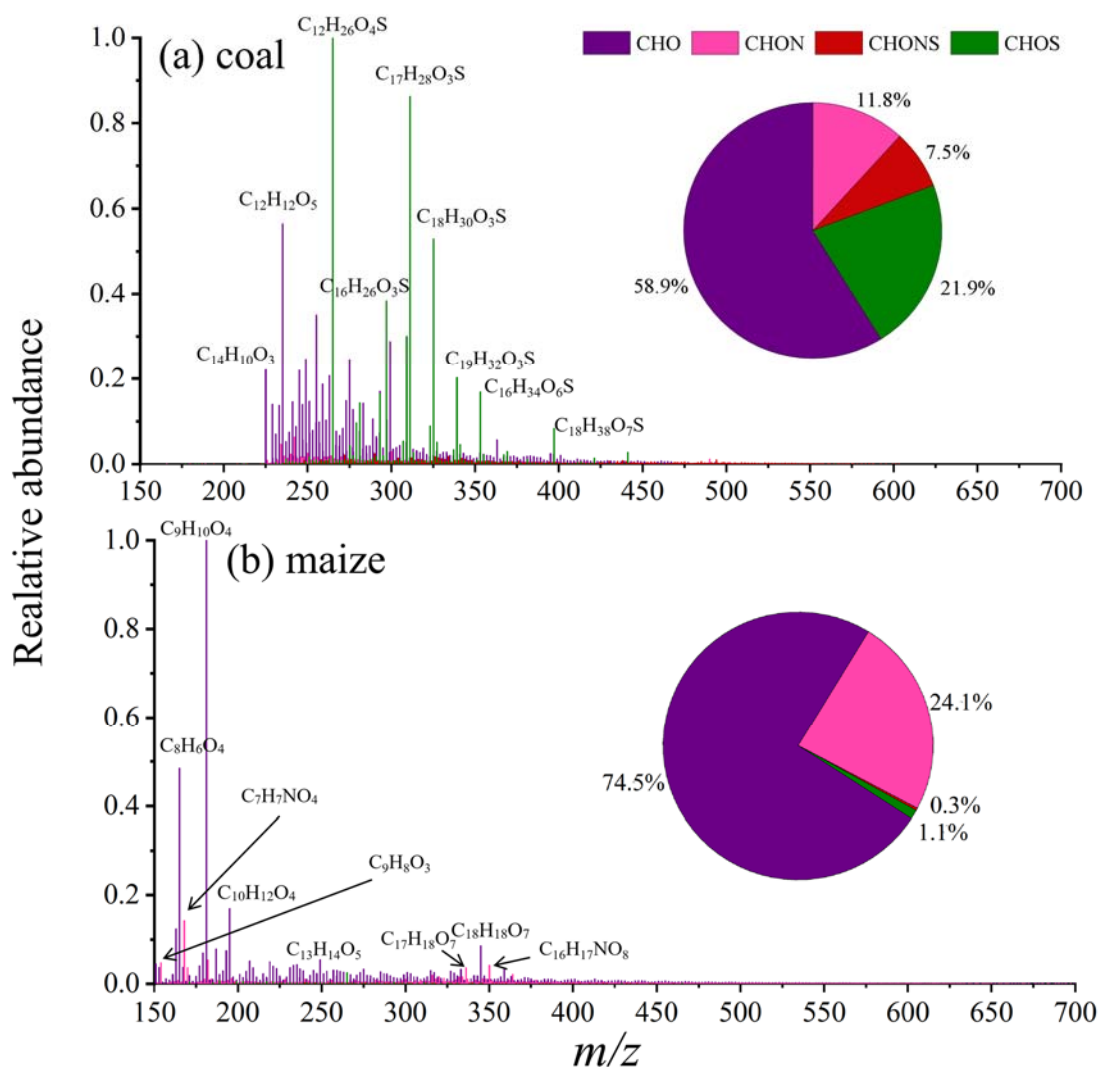
246 **3 Results and discussion**

247 **3.1 Comparison of fresh coal and maize smoke WSOM**

248 Fig. 1 showed the reconstructed FT-ICR mass spectra of WSOM for two fresh
249 extracts samples. Based on the intensity of each negative ion, the average molecular
250 formulas for coal and maize smoke extracts calculated as $\text{C}_{18.0}\text{H}_{24.0}\text{O}_{6.9}\text{N}_{0.90}\text{S}_{0.41}$ and
251 $\text{C}_{21.0}\text{H}_{21.7}\text{O}_{7.4}\text{N}_{0.86}\text{S}_{0.04}$, respectively, showing higher C in maize smoke extracts,
252 consistent with previous finding (Fan et al., 2016). In this study, these identified
253 molecular formulas were classified into four main compound groups based on their
254 compositions: CHO, CHON, CHOS, and CHONS. The relative abundances of the four

255 groups were determined by normalizing the magnitude of each peak to the total
256 magnitude of all identified peaks. Most peaks were located within the m/z range of 200–
257 400. The greatest peak magnitudes were mainly distributed within the m/z range of 250
258 –350. Distinct peak distribution patterns were observed for both smoke extracts. For
259 example, several CHOS compounds with high relative abundance, such as $C_{12}H_{26}O_4S$,
260 $C_{17}H_{28}O_3S$, $C_{18}H_{30}O_3S$, were identified in the coal smoke extract, whereas the high-
261 abundance CHO and CHON compounds, including $C_8H_{10}O_4$, $C_7H_7NO_4$, and $C_{18}H_{18}O_7$
262 were predominant in the maize smoke extract. It should be noted that peak magnitude
263 is not indicative of a compound's concentration in a sample due to inherent biases of
264 C18 extractions and electrospray ionization efficiencies.

265 To better illustrate the differences in the \bullet OH oxidation behavior between the
266 two extracts, the concentrations of inorganic ions and transition metals (Fe and Cu) in
267 the fresh WSOM were also measured, as shown in Table S1. It can be seen that the
268 concentrations of Cl^- and NH_4^+ ions in maize were much higher than those in coal,
269 whereas the concentration of SO_4^{2-} ions in coal was higher than that in maize. During
270 the photochemical reaction, the concentrations of these ions showed little change. In
271 addition, the concentrations of Fe and Cu ions were very low, almost below the
272 detection limits of the instrument. These results indicate that the influence of ions on
273 the photochemical reaction can be neglected, especially that of Fe and Cu.



274

275 **Fig. 1.** Reconstructed ESI(-) FT-ICR mass spectra of (a) coal and (b) maize smoke extracts colored
 276 by formula groups. The inserted pie charts show the percentage of four formula groups by intensity.

277

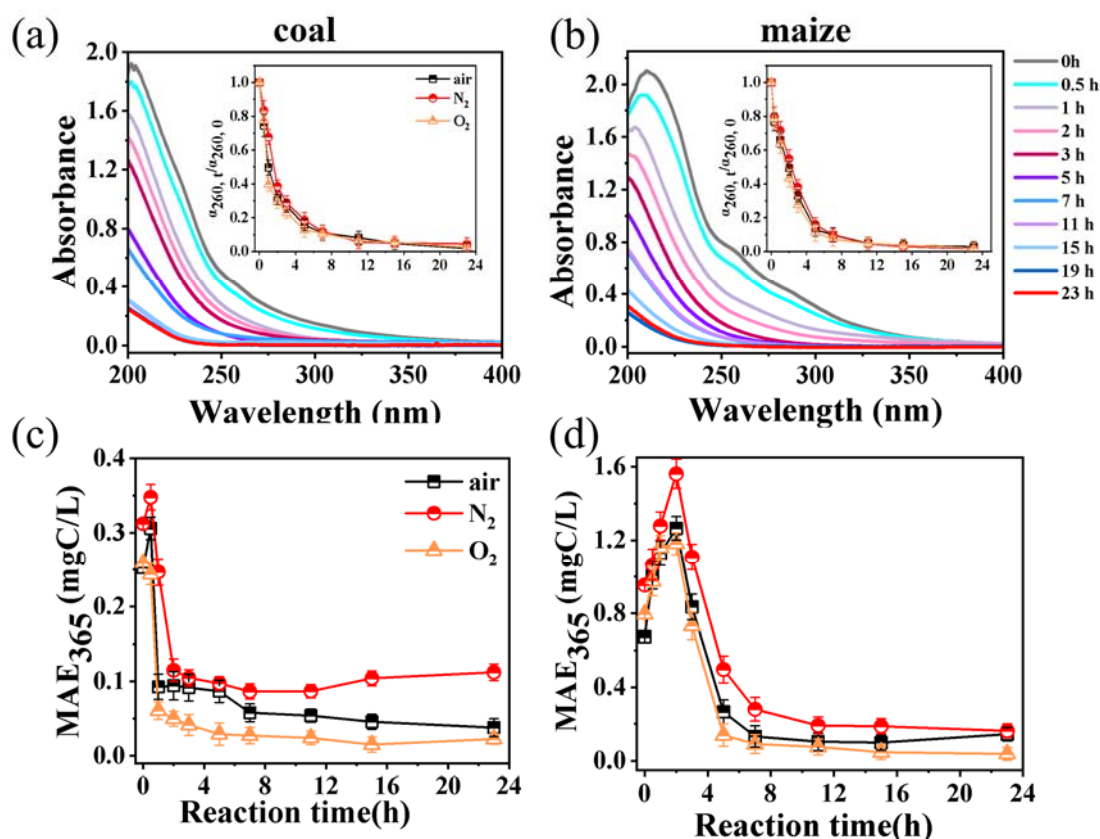
278 3.2 Optical properties during photooxidation of smoke extracts

279 3.2.1 Absorbance characteristics

280 Aqueous •OH oxidation of two smoke extracts—involving both photolysis and
 281 ROS oxidation reactions—can markedly alter their optical properties by degrading
 282 existing chromophores or generating new light-absorbing compounds. Fig.2 (a, b)
 283 shows the UV-vis absorbance spectra in the range of 200-500 nm of the reaction

284 solutions at varying irradiation time. Although the spectra were generally broad and
285 featureless, noticeable differences in the absorption intensity were observed between
286 coal and maize smoke. A distinct shoulder at 260 nm was observed in the spectra of
287 maize smoke WSOM, attributed to π - π^* transitions of unsaturated double bonds (e.g.,
288 C=C and C=O) (Li et al., 2021), indicating the presence of fulvic acid-like
289 chromophores. As the reaction progressed, overall decreases in absorbance (Fig. 2)
290 were observed for both smoke extracts, which can be ascribed to the degradation of
291 compounds containing carbonyl- and double bond groups. Tomaz et al. (2018) similarly
292 reported that aqueous \cdot OH oxidation of complex BB mixtures led to rapid depletion of
293 phenolic compounds and formation of small organic acids. Consistent with these
294 findings, photobleaching (i.e. decrease in light absorbance) is the most common effect
295 observed upon irradiation of SOA or BrC in the aqueous phase (Jiang et al., 2023). The
296 decreased light absorption was likely due to competing processes, including the
297 formation of light-absorbing products and fragmentation yielding less absorptive
298 compounds. Study by Chen et al. (2025) on molecular structure-dependent light
299 absorption demonstrated that CHO compounds with low molecular weight and high
300 aromaticity are primarily responsible for absorption in the 200–300 nm range, whereas
301 CHON compounds (mainly nitroaromatics) and highly aliphatic structures play a
302 dominant role in absorption above 365 nm. However, the present results differ from
303 recent studies on aqueous SOA formation from the photooxidation of coal and rice
304 straw smoke WSOM, which reported photoenhancement at wavelength above 360 nm
305 (Cao et al., 2025). Such discrepancies may be attributed to differences in light sources,

306 •OH concentrations, and the molecular composition of the smoke extracts. Clearly,
 307 different classes of compounds in smoke extracts exhibit distinct photochemical aging
 308 behavior, including photoenhancement, photobleaching or a combination of both.



309
 310 **Fig. 2.** (a, b) The UV-vis absorption spectra under different irradiation time for coal and maize
 311 smoke extracts, and (c, d) MAE at 365 nm over photoaging time. The inset shows the change in
 312 absorbance at the wavelength of 260 nm compared to the spectra at time zero.

313
 314 Changes in MAC₃₆₅ are commonly used to track chromophore evolution since different
 315 chromophores exhibit varying light-absorbing ability. Fig. 2(c, d) shows the variation
 316 of the MAC₃₆₅ over reaction time for both smoke extracts. For both smoke extracts,
 317 MAE₃₆₅ initially increased and then declined. The enhancement in light-absorbing can
 318 be mainly ascribed to two factors (Jiang et al., 2021). First, OH-addition to aromatic

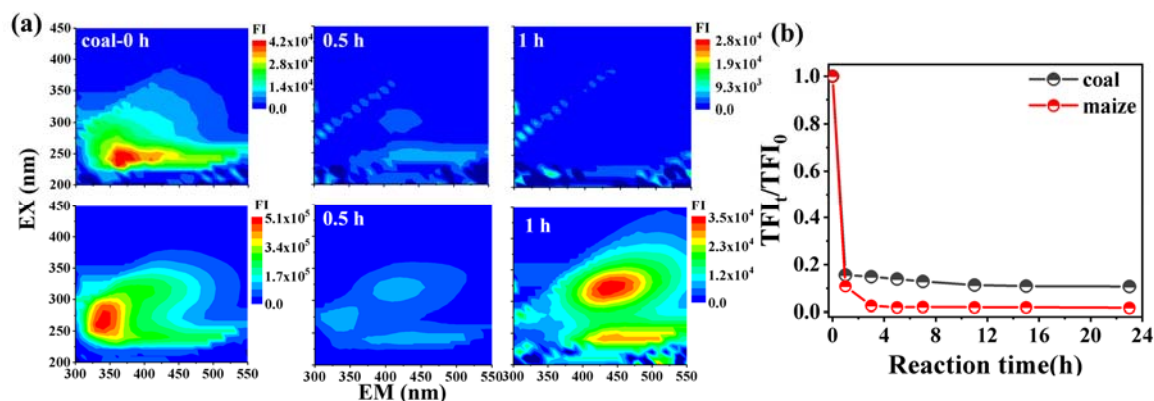
319 rings produces OH-rich compounds that act as chromophores (Lei et al., 2024). Second,
320 the formation of dimers and larger oligomers extends π -conjugation, shifting absorption
321 to longer wavelengths and enhancing light absorption. Generally, increased
322 functionalization and oligomerization increased light absorption (Go et al., 2024; Vione
323 et al., 2019). As the reaction proceeds, these intermediate chromophores transform into
324 smaller, ring-opened molecules with weaker or negligible light absorption. The
325 aqueous-phase photoaging of phenolic SOA also showed that light-absorbing properties
326 of oxidation products were strongly time-dependent (Jiang et al., 2023). Additionally,
327 photodegradation of WSOM can generate more volatile products, and their evaporation
328 may reduce WSOC (Fig. S1), thereby influencing the light absorption per unit C mass.
329 The final decrease in MAE₃₆₅ can also be supported by the FT-ICR MS results (see Sect.
330 3.3). The observed decrease in lignin-like fractions, together with reductions in DBE
331 and AI values, suggests the breakdown of these conjugated systems during aqueous
332 photooxidation, leading to a decline in MAE₃₆₅. Meanwhile, the formation of more
333 saturated compounds (e.g., lipid- and aliphatic-like species) further contributes to the
334 decrease in MAE₃₆₅. In addition, the formation of small oxygenated CHO species (e.g.,
335 carboxylic acids or CHO₂⁺ fragments from HR-AMS) with negligible absorbance at
336 365 nm dilutes the overall light-absorbing capacity. Another spectral parameter, E2/E3
337 (the ratio of absorbance at 250 nm to that at 365 nm), further characterizes these changes.
338 During the first hour of •OH oxidation, E2/E3 decreased from 16 to 8 for coal smoke,
339 indicating enrichment in high-molecular-weight chromophores with stronger light-
340 absorbing capability. However, it increased from 12 to 22 for maize smoke extracts (Fig.
341 S2). These contrasting E2/E3 trends highlight distinct molecular transformations in
342 WSOM for coal and maize smoke under •OH photooxidation.

343 **3.2.2 Fluorescence properties**

344 Fluorescence spectra provide more detailed molecular information than UV-vis
345 spectra. For example, a red shift in the excitation–emission maximum typically
346 indicates increased aromaticity and higher molecular weight (Tang et al., 2020). Fig. 3a
347 presents the EEM spectra of both smoke samples upon irradiation. We observed a rapid
348 decrease in the characteristic fluorescence peak (Ex/Em = 275/350 nm) within the first
349 hour of the reaction. Concurrently, two new fluorescence peaks emerged at Ex/Em =
350 325/400–500 nm and 225/400–500 nm, indicating the formation of humic-like
351 chromophores. As the reaction progressed, the intensities of these newly formed peaks
352 gradually declined. Consistently, HULIS-C concentrations increased during the initial
353 1–3 h for both smoke extracts, followed by a gradual decrease over time (Fig. S3). As
354 shown in Fig. 3b, the total fluorescence intensity (Ex = 250–450 nm, Em = 300–650
355 nm) decreased sharply within the first hour and then declined at a slower rate thereafter.

356 The HIX, BIX and FI were further employed to evaluate the degree of humification
357 and freshness of organic matters. As suggested by Wu et al. (2021), an increased in HIX
358 accompanied by decrease in BIX and FI can serve as indicators of enhanced oxidation
359 of atmospheric WSOC. As shown in Fig. S4, the HIX value increased during the first
360 hour and then decreased, suggesting that the formation of humic-like substances
361 initially exceeded their subsequent degradation. Conversely, FI and BIX values
362 decreased at the early stage of oxidation for both smoke samples (Fig. S4). In general,
363 greater humification is associated with lower protein content, primarily due to a
364 reduction in carbon-hydrogen compounds and a red shift in the fluorescence emission
365 wavelength of more humified molecules. Conversely, a higher BIX indicates a higher

366 contribution from protein-like and amino acid components.



367

368 **Fig. 3.** (a)Variation trend of EEM fluorescence spectra and (b) temporal profiles of total

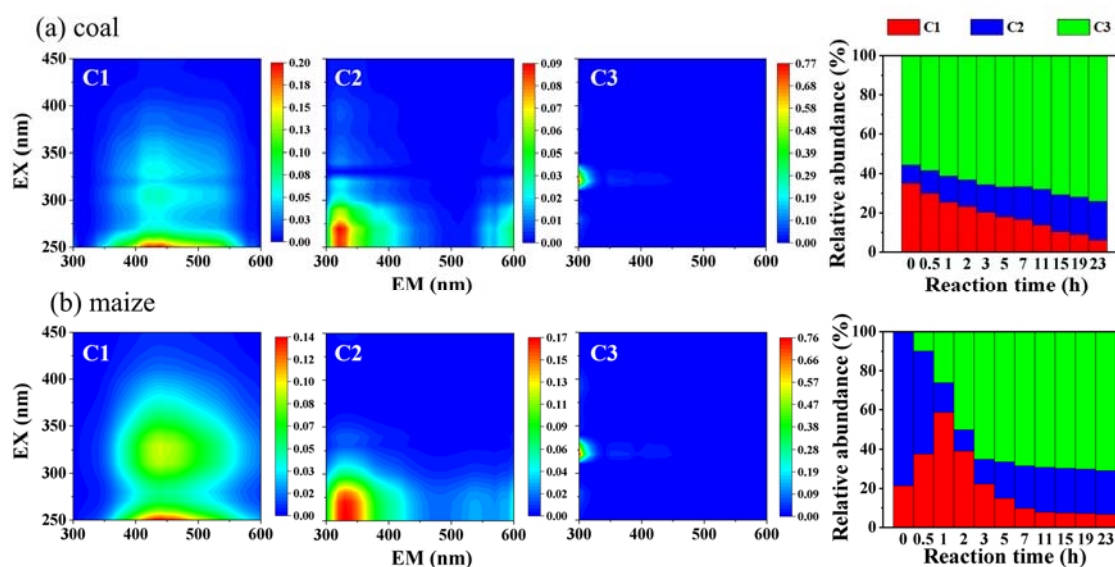
369 fluorescence intensity for two smoke extracts.

370

371 The PARAFAC model identified three underlying fluorescent components,
372 including one humic-like components (C1) and two protein-like component (C2 and
373 C3) (Fig. 3). Component C1 is considered to be a humic-related substance,
374 characterized by two peaks at Ex/ Em=230/400–500 nm and 300/400-500 nm (Huang
375 et al., 2025). C2 displays peaks at Ex/Em=250-300/300-350 nm, which can be
376 attributed to tyrosine-like components. C3 (Ex/Em=325/300 nm) is likely link to
377 tryptophan-like components. As shown in Fig. 4, the proportion of C1-C3 in both maize
378 and coal WSOM varied dynamically throughout photochemical processes. For coal
379 WSOM, C1 fraction decreased, whereas C2 and C3 increased. In contrast, for maize
380 WSOM, C2 gradually transformed into C1 at the first hour, resulting in opposite trends
381 between the two components. This transformation likely reflects the formation of more
382 oxygenated humic-like substances via OH-functionalization at the early stage,
383 consistent with change trends of Hulis-C for maize smoke extracts (Fig. S3). This

384 interpretation can be further confirmed by the increase in HIX values for maize smoke
385 during the first hour of photooxidation (Fig. S4 c).

386 For both smoke WSOM samples, the C3 component exhibited a gradual increase
387 over time. The findings are in accordance with other's study on the photooxidation of
388 WSOC emitted from rice straw combustion (Zhang et al., 2021). The stronger
389 fluorescence intensity observed at Ex/Em=325/300 nm may correspond to low-ring
390 PAHs and their derivatives, which are known to be produced in abundance during
391 biomass pyrolysis or burning (Mahamuni et al., 2020). Overall, the EEM components
392 varied depending on the types of smoke-derived WSOM.



393

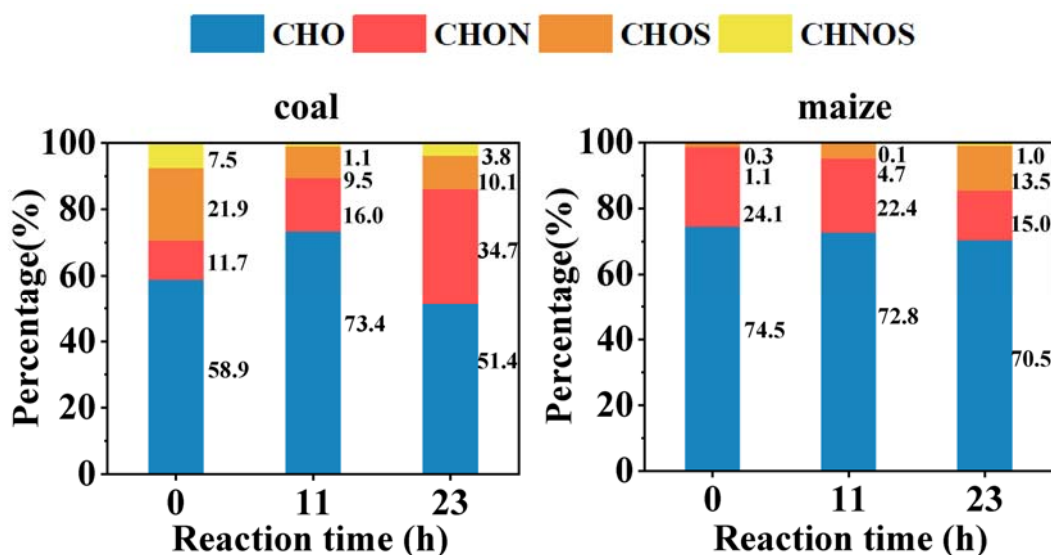
394 **Fig. 4.** Three fluorescent components (C1-C3) of the smoke extracts identified by the EEM-
395 PARAFAC model and variations in the relative contributions of each PARAFAC component of (a)
396 coal and (b) maize smoke extracts with photoaging time.

397

398 3.3 Molecular composition of WSOM via FT-ICR MS

399 The intensity weighted average values of various molecular parameters—including
400 molecular weight (MW), elemental ratios (H/C and O/C), DBE, AI—for maize and coal
401 smoke extracts before and after photoaging were summarized in Table 1. As listed in

402 Table 1, a total number of 5596 and 5107 molecular formulas were identified for fresh
403 coal and maize extracts, respectively, within the m/z range of 100-600, indicating the
404 complicated molecular compositions of WSOM. For coal WSOM, the MW decreased
405 slightly 313 g/mol in the fresh sample to 296 and 288 after 11 h and 23 h photooxidation,
406 respectively. The MW for maize remained nearly unchanged during OH-photooxidation.
407 The dominant species in both smoke extracts were CHO and CHON compounds, with
408 higher abundance observed in maize than in coal smoke extract (Fig. 5). Molecular
409 composition analysis further revealed that maize smoke WSOM was largely composed
410 of CHO and CHON, together accounting for 98.6% of the total peak area. CHO
411 compounds constituted more than half of all identified molecular formulas in both
412 WSOM samples (74.5% for maize and 58.9% for coal). In contrast, S-containing
413 compounds (CHOS and CHONS) were much more abundant in coal smoke extracts
414 (29.4% in total) than in maize (1.4% in total). Similarly, previous studies reported that
415 the fractions of S-containing CHOS and CHONS species in crop-derived WSOM were
416 relatively low (3-9% in peak area) (Li et al., 2024). Interestingly, S-containing
417 compounds in coal smoke decreased by nearly 50% after photodegradation, whereas
418 their abundance increased markedly in maize smoke extracts. Meanwhile, the
419 proportion of CHON compounds in coal smoke increased under photoaging, which may
420 be attributed to the photochemical transformation of CHONS species and/or the
421 oxidation of reduced CHN compounds. Conversely, the CHON proportion in maize
422 smoke decreases with reaction time, likely due to the progressive degradation of
423 nitroaromatic compounds commonly present in biomass burning emissions (Lin et al.,
424 2016).



425

426 **Fig. 5.** Change of relative abundance fraction of four groups (CHO, CHON, CHOS, and CHONS)

427 with reaction time in both smoke extracts.

428 The molecular-level parameters are summarized in Table 1. DBE values ranged

429 from 2 to 9 for coal-smoke WSOM and from 2 to 11 for maize-smoke WSOM. The

430 degree of unsaturation and aromaticity of molecular formulas can be valued using the

431 H/C ratio and DBE values, with lower H/C ratios and higher DBE indicating greater

432 unsaturation and, to some extent, stronger aromatic character. As shown in Table 1, after

433 23 h of photooxidation, aged WSOM exhibited higher H/C ratios (1.75 vs. 1.32 for coal;

434 1.68 vs. 1.02 for maize), lower DBE values (3.85 vs. 7.12 for coal; 4.08 vs. 8.99 for

435 maize), and reduced AI values (0.16 vs. 0.31 for coal; 0.16 vs. 0.48 for maize) compared

436 to the fresh samples. These concurrent changes consistently indicate the breakdown of

437 aromatic structures and an overall shift toward more saturated compounds. This trend

438 agrees with previous findings from dark aqueous \bullet OH oxidation of BB smoke WSOC

439 reported by Fan et al. (2024).

440 At the molecular-class level, CHON compounds in maize smoke initially exhibit a

441 relatively high average molecular weight (MW, 329.45 g/mol) and DBE (10.52). Upon
442 photolysis, the average MW decreases to 301.07 g/mol (11 h) and 296.44 g/mol (23 h),
443 while the DBE declines to 6.59 and 4.14, respectively. These changes reflect the
444 progressive breakdown of conjugated structures and a corresponding reduction in
445 aromaticity, consistent with the observed decrease in light absorbance (Fig.2 b). For
446 coal smoke, a considerable fraction of CHONS species undergoes transformation into
447 CHON compounds with lower aromaticity and DBE during photolysis. This conversion
448 increases the relative abundance of CHON species while contributing to a decrease in
449 overall molecular weight. In addition, the MW of CHO compounds in coal smoke
450 decreases progressively with photolysis. In contrast, maize-smoke WSOM is
451 dominated by CHO compounds, whose MW remains relatively unchanged during
452 photolysis, resulting in only minor variation in the bulk molecular weight. This contrast
453 primarily reflects differences in the initial WSOC compositions between coal and maize
454 smoke. Overall, the marked decreases in AI and DBE for CHON compounds in both
455 smokes indicate substantial loss of aromaticity, which in turn contributes to the
456 reduction in light absorption.

457 Additionally, the O/C increased from 0.38 to 0.45 for coal and from 0.40 to 0.55
458 after 11 h of oxidation, followed by a decrease to 0.27 and 0.25 at 23 h, respectively.
459 This trend indicates a transformation from OH-functionalization to fragmentation as
460 photooxidation progressed. A decrease in DBE per carbon (DBE/C) was observed after
461 23 h of photodegradation—from 0.45 to 0.25 for coal and 0.62 to 0.27 for maize—
462 further confirming the transformation of refractory aromatic-condensed structures into
463 more polar and readily degradable small molecules. Fig. S5 shows the relationship

464 between DBE values and C atom numbers for four compound groups identified by FT-
 465 ICR MS.

466 **Table 1** Intensity-weighted average molecular parameters (MW, elemental ratios, DBE, DBE/C, AI)
 467 of coal and maize smoke WSOM before and after ·OH photooxidation

Sample	Time	Elemental composition	Formulas number	MW (g/mol)	DBE	AI	O/C	H/C	DBE/C
coal	0 h	Total	5596	312.98	7.12	0.31	0.38	1.32	0.45
		CHO	1728	300.23	8.16	0.38	0.36	1.16	0.52
		CHON	1695	323.12	8.77	0.43	0.49	1.25	0.54
		CHOS	702	310.03	3.60	0.10	0.31	1.74	0.23
		CHONS	1471	406.27	6.61	0.19	0.55	1.48	0.41
	11 h	Total	5157	296.35	4.58	0.17	0.45	1.57	0.34
		CHO	2066	286.35	4.61	0.16	0.47	1.54	0.35
		CHON	2029	312.31	4.10	0.16	0.40	1.68	0.31
		CHOS	816	343.04	4.93	0.16	0.29	1.62	0.29
		CHONS	246	329.73	6.45	1.01	0.86	1.63	0.54
	23 h	Total	5072	288.32	3.85	0.16	0.27	1.75	0.25
		CHO	1348	262.69	4.04	0.15	0.26	1.66	0.28
		CHON	1970	304.36	2.03	0.07	0.25	1.99	0.14
		CHOS	723	313.19	4.80	0.17	0.31	1.67	0.27
		CHONS	1031	398.63	7.04	0.33	0.52	1.63	0.39
maize	0 h	Total	5107	286.90	8.99	0.48	0.40	1.02	0.62
		CHO	2143	273.62	8.56	0.46	0.40	1.02	0.61

	CHON	2772	329.45	10.52	0.54	0.40	0.98	0.66
	CHOS	107	248.21	4.61	0.22	0.46	1.37	0.47
	CHONS	85	317.32	7.31	0.28	0.56	1.13	0.61
<hr/>								
	Total	6027	288.84	5.44	0.21	0.55	1.40	0.44
	CHO	2643	283.95	5.19	0.19	0.56	1.41	0.42
11 h	CHON	2954	301.07	6.59	0.30	0.57	1.29	0.54
	CHOS	395	305.41	3.69	0.12	0.35	1.83	0.20
	CHONS	35	317.42	10.37	0.45	0.23	1.19	0.54
<hr/>								
	Total	5147	285.81	4.08	0.16	0.25	1.68	0.27
	CHO	2647	277.01	4.20	0.16	0.23	1.65	0.27
23 h	CHON	1995	296.44	4.14	0.19	0.28	1.69	0.30
	CHOS	400	312.24	2.94	0.09	0.34	1.86	0.18
	CHONS	105	393.70	10.63	1.03	0.49	1.11	0.67

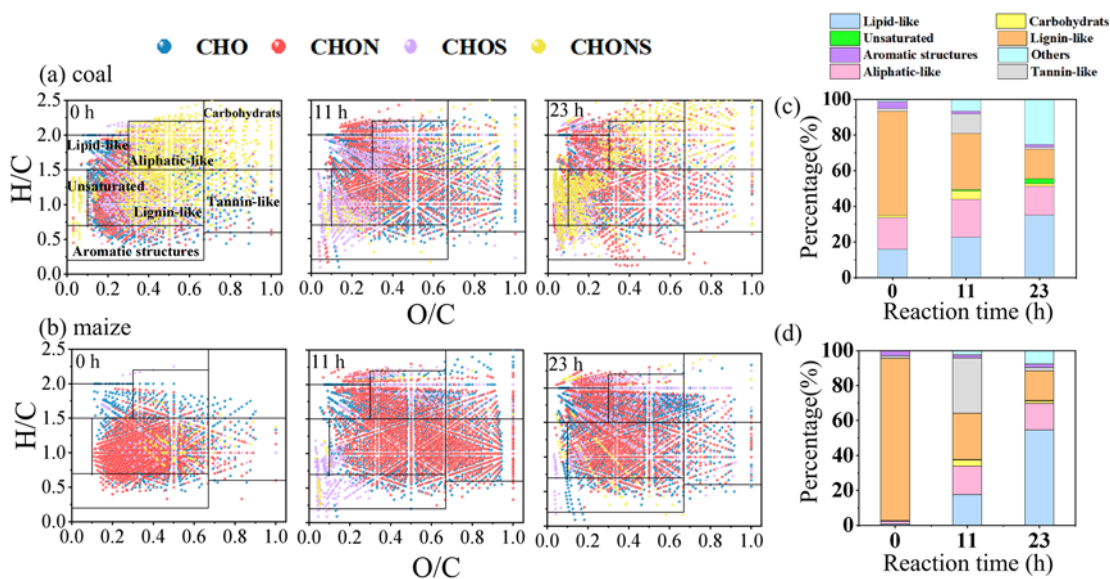
468

469 The van Krevelen diagram (Fig. 6), which plots the O/C ratio as the x-axis and the
470 H/C ratio on the y-axis, was used to elucidate the molecular distribution. For clarity, the
471 corresponding detailed values were listed in Table S2. Lignin-like compounds
472 dominated both coal and maize smoke WSOM, accounting for 58.2% and 93.1% of
473 total intensity, respectively, indicating a greater abundance of phenolic organic species
474 in maize smoke. Previous study also showed that CHO formulas were mainly lignin-
475 pyrolysis products (Song et al., 2018). After photoaging, the lignin-like fraction
476 decreased significantly, reflecting the degradation of aromatic phenolic species. Given
477 that most lignin-like compounds possess strong light-absorbing properties, their

478 decomposition directly contributed to the observed decrease in absorbance. In contrast,
479 the intensity of saturated compounds (sum of lipids and aliphatic components)
480 increased substantially after OH-induced photooxidation, from 33.8 % to 51.2% at 23
481 h for coal and from 2.4% to 69.8 % for maize. These observations suggest a significant
482 increase in saturated aliphatic and O-enriched compounds after •OH photooxidation.

483 As listed in Table S2, the initial increase followed by a decrease (from 11.2% to
484 1.1% for coal and 31.8% to 2.1% for maize smoke) in tannin-like compounds suggests
485 that radical coupling, condensation, or addition reactions likely occurred during the
486 early stage of the reaction, leading to a higher O/C ratio at 11 h compared to the fresh
487 sample.

488 Condensed aromatic molecules, characterized by low H/C and O/C ratios but high
489 AI, showed a slight decrease with photoaging, indicating the partial degradation of
490 highly aromatic structures. Overall, the reduction in aromatic and lignin-like
491 compounds aligns with the observed decline in the light-absorbing properties (see Sect.
492 3.2.1). In all, aromatic and lignin-like compounds were continuously transformed into
493 lipid- and aliphatic-like compounds. During the initial stage (first 5 h), carbohydrate-
494 like substance such as oxalate were generated (Fig. S6), but their abundance
495 subsequently decreased, consistent with the pH variation that first declined (initial 3 h)
496 and then increased again (Fig. S7). The formation of carboxylic acids can be further
497 confirmed later by identifying their characteristic fragment ions using HR-AMS.



498

499 **Fig. 6.** (a, b) Van Krevelen diagrams of four groups (CHO, CHNO, CHOS, and CHNOS) and (c, d)

500 Intensity-weighted fractions of seven major molecular classes. Saturated compounds represent the

501 sum of lipid-like and aliphatic components. Unsaturated represents unsaturated hydrocarbons.

502

503 To further elucidate the photooxidation behaviors of both smoke extracts, the

504 number proportions of resistant, degraded and newly produced molecules were

505 summarized in Table S3. After 11 h of irradiation, 55.1 % and 58.2% of the total

506 formulas in fresh coal and maize, were degraded, resulting in 51.3% and 64.6% newly

507 formed formulas. From 11 h to 23 h, the numbers of newly produced and degraded

508 molecules increased slightly for coal but decreased for maize. Fig. 7 illustrates the O/C

509 vs. H/C distributions of degraded and newly formed compounds after 11 h and 23 h of

510 photodegradation. For coal, most degraded compounds were located in high O/C

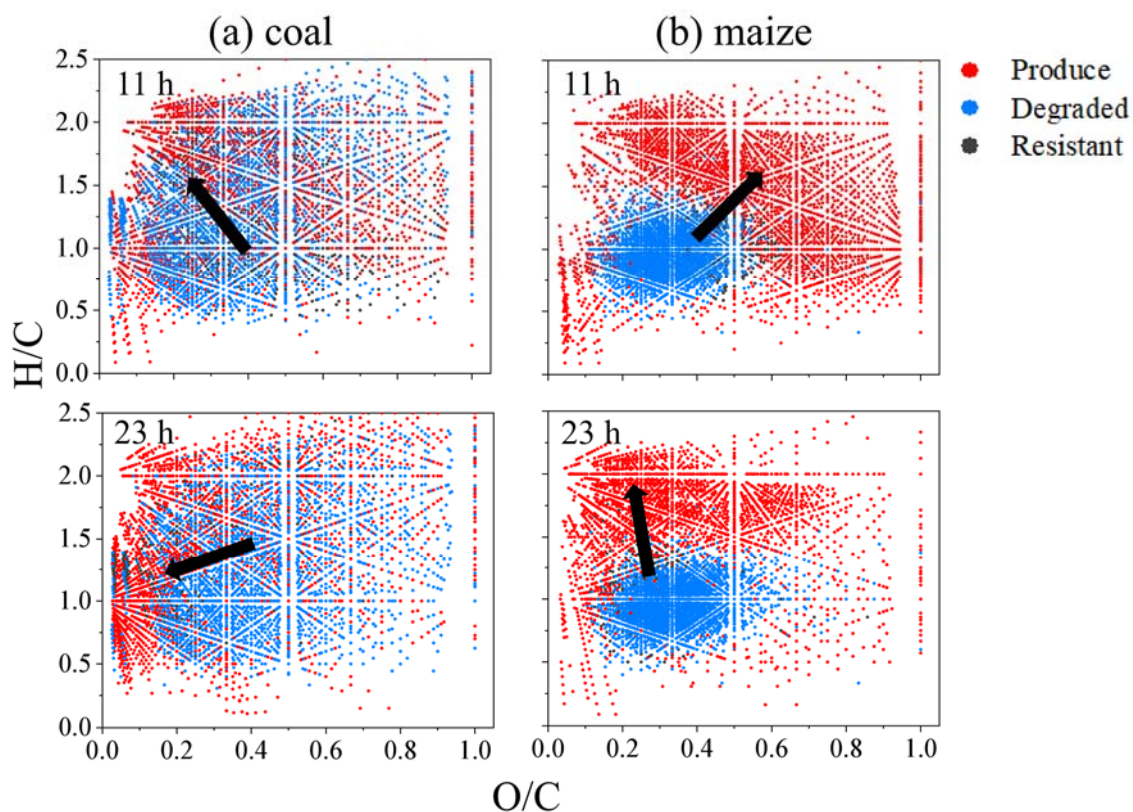
511 regions, whereas some newly formed species with much lower O/C and higher H/C

512 were likely associated with unsaturated hydrocarbons and lipid-like species. In contrast,

513 maize exhibited a marked shift from low to high O/C and H/C compounds at 11 h,

514 resulting in an increase in average O/C ratio. This trend suggests that maize compounds
515 mainly underwent functionalization during the first stage — introducing oxygen-
516 containing groups without breaking the carbon skeleton, thereby increasing O/C and
517 slightly lowering or maintaining H/C. The shift toward higher O/C ratios in the van
518 Krevelen diagram further supports the progression from aromatic to more oxygenated
519 and saturated compounds for maize smoke WSOM.

520 Overall, these results reveal distinct degradation pathways and product
521 characteristics for coal and maize smoke extracts.



522

523 **Fig. 7.** Van Krevelen diagrams of resistant, degraded and produced formulas in WSOM derived
524 from (a) coal and (b) maize burning before and after OH photooxidation.

525 3.4 AqSOA composition and mass yield

526 The aqSOA spectra exhibited higher mass fractions of $C_xH_y^+$ and $C_xH_yO_1^+$ ions

527 but lower fractions of $C_xH_yN_p^+$ and $C_xH_yO_xN_p^+$ ions (Fig. 8). For corn-derived aqSOA,
528 the fractions of $C_xH_y^+$ and $C_xH_yO_1^+$ both decreased by approximately 10% with
529 increasing photolysis time, while $C_xH_yO_2^+$ increased substantially from 15.95% to
530 29.96% after 23 h of photoreaction. In contrast, for coal-derived aqSOA, the fraction
531 of $C_xH_yO_1^+$ increased with irradiation time, while no corresponding increase in
532 $C_xH_yO_2^+$ was observed. This suggests that the overall oxidation degree of coal-derived
533 aqSOA did not increase significantly relative to that prior to irradiation.

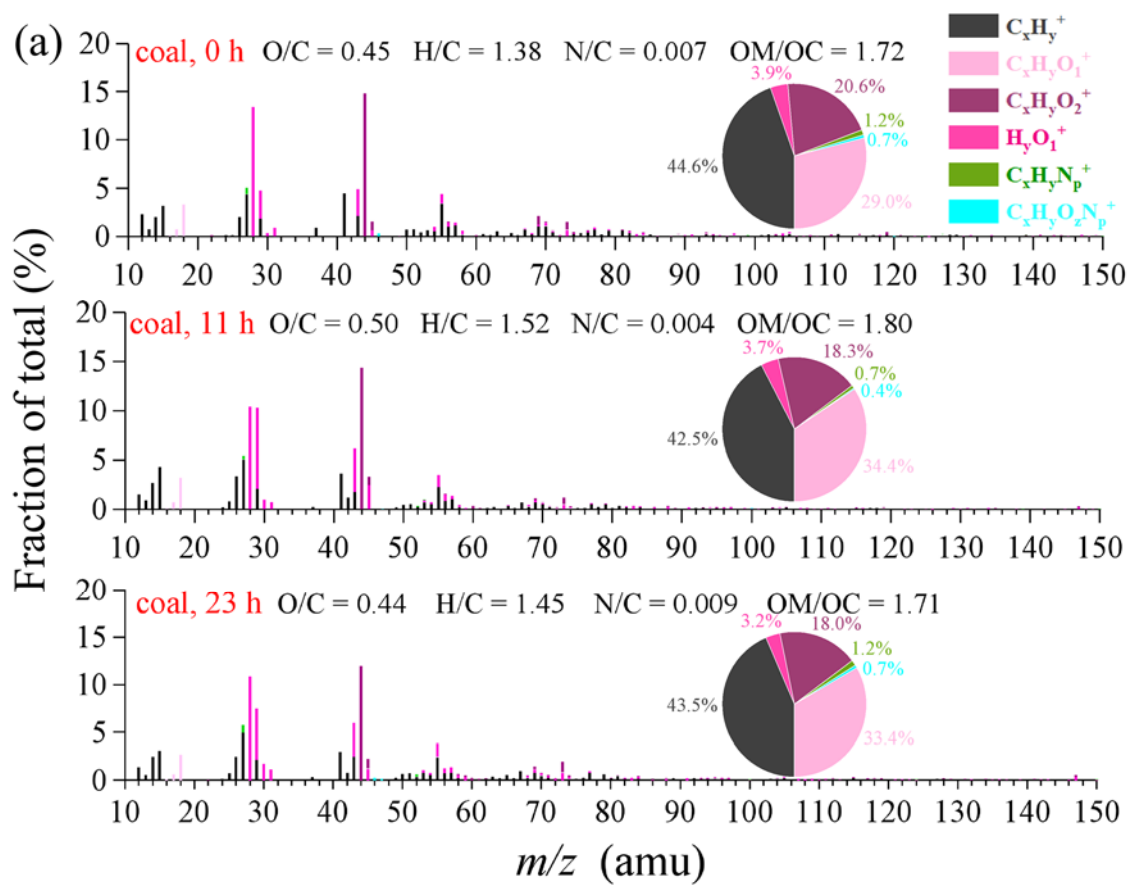
534 Table S4 summarizes the chemical properties, mass concentration and yield of the
535 formed aqSOA and their evolution during the photoreaction. During the first 5 -7 h,
536 both f_{44} and OSc values increased, indicating a progressive enhancement in the
537 oxidation state of aqSOA for both samples. In contrast, the H/C ratio exhibited only
538 minor changes throughout the reaction, suggesting relatively stable bulk hydrogen
539 content despite ongoing oxidation. A comparison between the two systems further
540 reveals that maize-derived aqSOA undergoes a more pronounced increase in oxidation
541 at the early stage, likely driven by functionalization reactions. As photochemical
542 processing continues, however, a slight decline in oxidation is observed, which can be
543 attributed to fragmentation processes. This trend is less evident in coal-derived aqSOA,
544 highlighting differences in their underlying transformation mechanisms. Notably, the
545 significantly higher O/C ratios and OSc of maize-derived aqSOA compared to those of
546 the precursors suggest that aqueous-phase processing can serve as an effective source
547 of oxygenated SOA in regions influenced by biomass burning emissions. The value of
548 f_{43} remained relatively low value (less than 0.1) and is therefore not discussed further.

549 For coal samples, the aqSOA mass concentration ranged from 50.77 mg/L to
550 126.95 mg/L. It reached a minimum at 11 h and subsequently increased to 126.95 mg/L

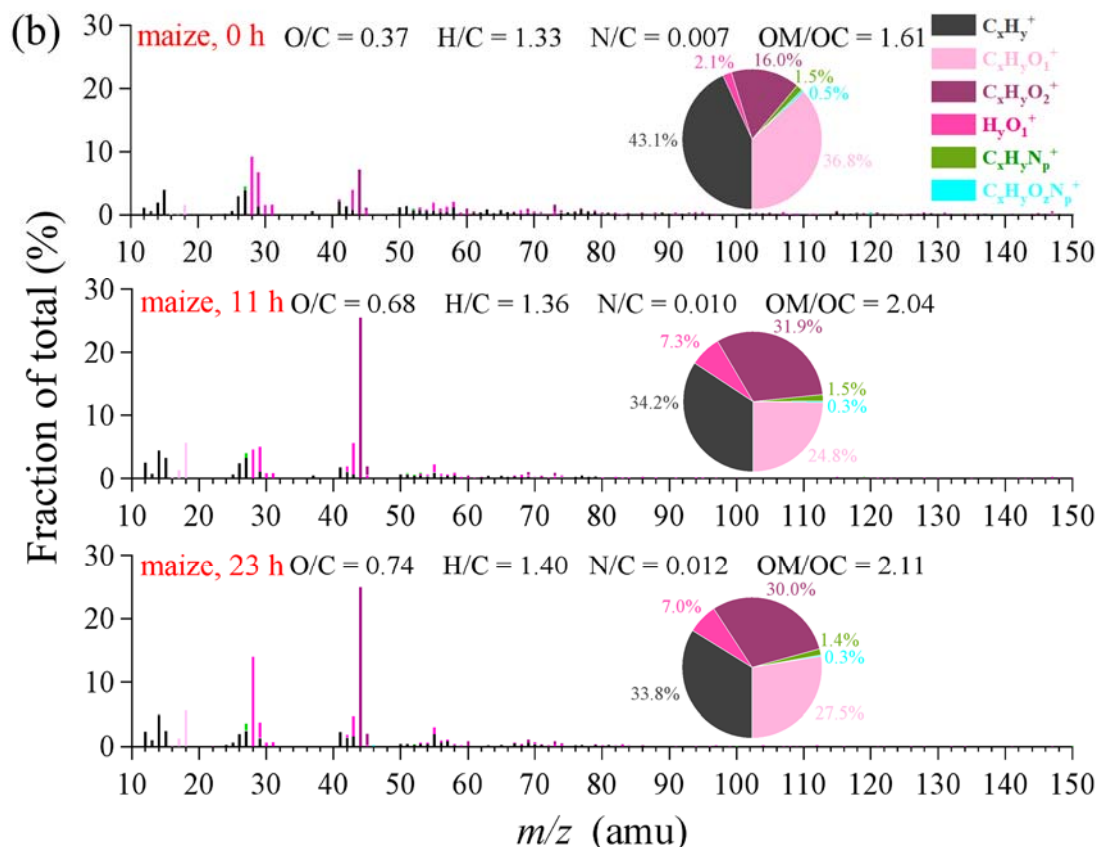
551 at 23 h. Correspondingly, the aqSOA mass yield peaked at 148.44% at 1 h, continuously
552 decreased to 1.87% within 9 h, and then increased again to 33.91% at 23 h. The aqSOA
553 mass yield of maize was significantly lower (less than 10%) than that of coal samples,
554 indicating that coal sample is more efficient at generating low-volatility species
555 compared to maize. The possible reasons why coal-derived aqSOA is higher than that
556 from maize are as follows. First, the fresh coal-derived CHOS compounds are
557 dominated by species such as $C_{17}H_{28}O_3S$ and $C_{18}H_{30}O_3S$, which are mainly
558 organosulfates. These compounds have relatively high saturation and stability, and
559 undergo little change upon photolysis, resulting in a high SOA mass yield measured by
560 HR-AMS. In contrast, maize-derived WSOM is primarily composed of lignin-like
561 substances with high DBE values, which are more susceptible to OH functionalization,
562 forming saturated fatty acids or polyhydroxy acids (e.g., $C_9H_{18}O_6$ and $C_9H_{10}O_7$). These
563 products can further undergo fragmentation into smaller, more volatile products (e.g.,
564 low-molecular-weight acids), leading to a lower aqSOA mass yield.

565 The significant formation of carboxylic acids during the first 9 h of photoreaction
566 is further evidenced by the Van Krevelen diagram (H/C versus O/C), in which aqSOA
567 evolves along a slope of approximately -1 throughout the photooxidation process (Fig.
568 S8). Consistently, the CHO_2^+ ion in the aqSOA AMS spectra—commonly used as a
569 tracer for carboxylic functional groups—exhibits a continuous increase during the first
570 5 h of photoreaction (Fig. S9). After 3–9 h of reaction, the concentration of CHO_2^+
571 decreases, accompanied by a decline in f_{44} . A plausible explanation is the occurrence
572 of fragmentation reactions, during which the oxidation products initially formed
573 through oligomerization or functionalization decompose into smaller, more oxidized
574 species. This trend has also been reported in previous studies on the photooxidation of

575 phenolic carbonyls (Jiang et al., 2021).



576



577

578 **Fig. 8.** High-resolution MS profiles for aqSOA products at 0 h, 11 h and 23 h for (a) coal and (b)
 579 maize. The peaks in the mass spectra are color-coded according to six ion categories: $C_xH_y^+$,
 580 $C_xH_yO_1^+$, $C_xH_yO_2^+$, $H_yO_1^+$, $C_xH_yN_p^+$ and $C_xH_yO_xN_p^+$ ions. The inserted pie charts denote the mass
 581 fraction of each ion family to the total MS.

582

583 3.5 DTT analysis

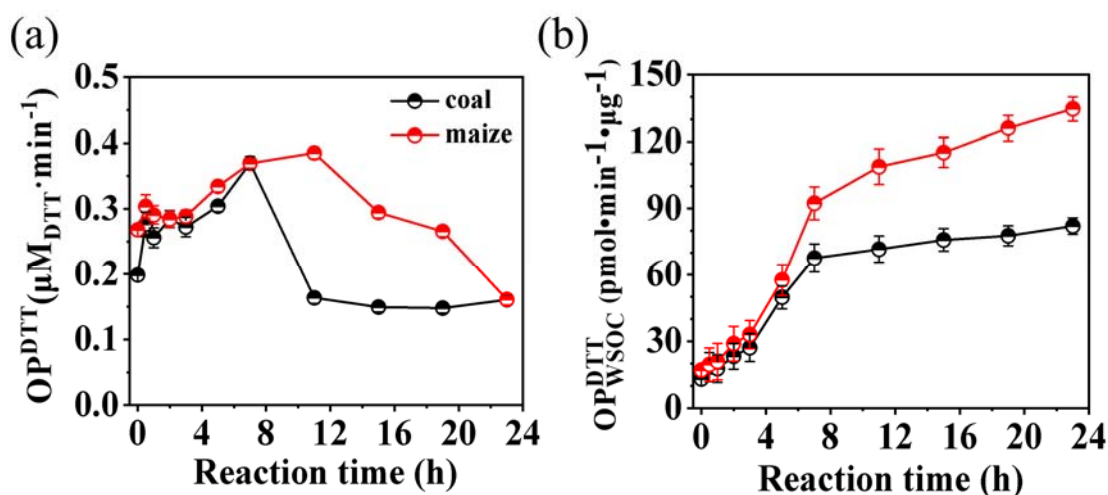
584 Aqueous photochemical aging of BB smoke can also alter its toxicity. The oxidative
 585 potential of the reaction solutions was evaluated using the dithiothreitol (DTT) assay,
 586 as described in our previous work (Ye et al., 2025). As shown in Fig. 9a, based on the
 587 DTT consumption rate (OP^{DTT}), OH-initiated photooxidation of smoke extracts led to
 588 an increase in OP^{DTT} during the first 1 h. Upon prolonged photoaging, the OP^{DTT} value
 589 decreased to $0.15 \mu\text{M DTT min}^{-1}$ after 23 h, slightly lower than the corresponding initial
 590 values. Previous research results also suggested that aqueous OH oxidation of WS-
 591 BBOA components generally leads to a final reduction in OP^{DTT} (Wong et al., 2019;
 592 Jiang and Jang, 2018) during prolong irradiation, consistent to our findings. The
 593 temporal variation pattern of OP^{DTT} is comparable to that observed for aqueous

594 oxidation of soybean straw extracts (Ye et al., 2025), but opposite to that of 4NC
595 photodegradation (Lei et al., 2025). The DTT activity is likely associated with light-
596 absorbing and fluorescent substances containing large conjugated electron systems,
597 which can transfer electrons to participate in catalytic reaction, thereby contributing to
598 DTT activity (Chen et al., 2019). The reduction in DTT activity after 23 h agrees with
599 the decrease of lignin-like and aromatic compounds revealed by FT-ICR MS analysis.

600 Given that aqueous OH oxidation did not significantly reduce the total WSOC
601 concentrations, the decrease in OP^{DTT} is likely attributed to the formation of non- or
602 less DTT-active components. However, total WSOC decreased significantly upon aging;
603 consequently, the OP^{DTT} normalized by WSOC increased over irradiation time,
604 suggesting the possible formation of secondary toxic organic species during the aging
605 processes. Previous published studies have also showed that photochemical aging of
606 fresh particles can either enhance or diminish toxicity, depending on their sources and
607 oxidation conditions (Fang et al., 2024). To further characterize the ROS-generation
608 potential of WSOM from different combustion sources, we calculated the WSOC-
609 normalized DTT consumption rate (OP_{WSOC}^{DTT} , OP^{DTT} divided by WSOC). The results
610 showed that the mass-normalized DTT consumption rates gradually increased and
611 reached a plateau at 132 and 82 pmol/min/ μ g for maize and coal smoke extracts,
612 respectively, similar to finding from Wong et al. (2019). These values are higher than
613 those reported for water extracts from PM_{2.5} aerosol (22-68 pmol·min⁻¹· μ g⁻¹) (Verma et
614 al., 2012). Based on the molecular-level differences after •OH photooxidation, the
615 reasons for the OP_{WSOC}^{DTT} changes induced by OH-photolysis in coal and maize are
616 likely different. For coal, the increase in OP_{WSOC}^{DTT} may primarily result from the
617 formation of CHON compounds after photolysis, whereas for maize, the increase is
618 probably due to the production of more quinone species or OH addition products during

619 the reaction (Tang et al., 2025; Wong et al., 2019).

620 Unfortunately, due to the limitations of current analytical techniques, it remains
621 challenging or even impossible to attribute the observed DTT variation trends to
622 specific molecular species.



623
624 **Fig. 9.** (a) Temporal evolution of DTT consumption rate and (b) WSOC-normalized DTT activity
625 for both smoke extracts during aqueous OH photooxidation.

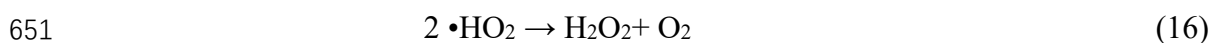
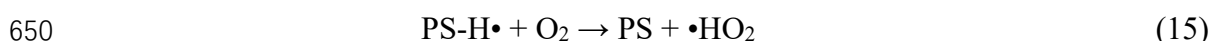
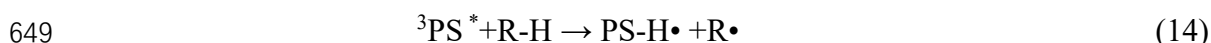
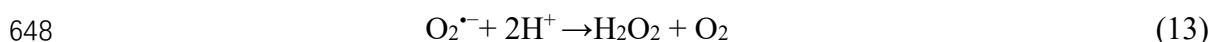
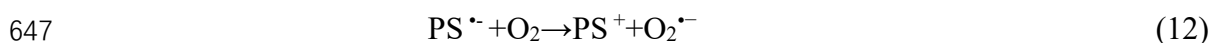
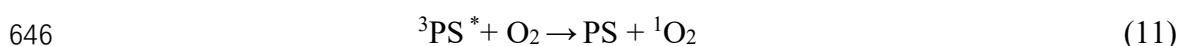
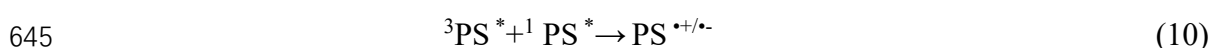
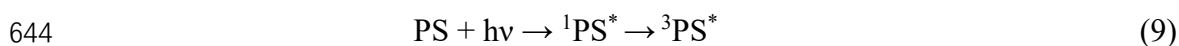
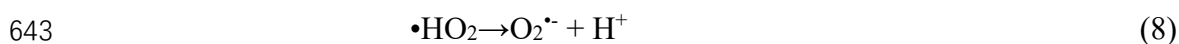
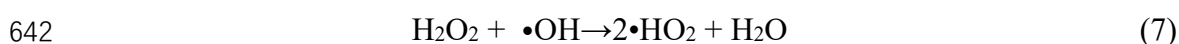
626 3.6 ROS contribution and reaction mechanism

627 3.6.1 ROS concentration and relative contribution

628 Hydrogen peroxide can undergo photolysis to generate $\bullet OH$, which effectively
629 break down chromophores, thereby decreasing light absorption. The OH radicals can
630 oxidize most organic species, leading to a sharp decrease in both WSOC and absorbance
631 during the initial reaction stage.

632 According to previous studies (Arciva et al., 2022), when the concentration of the
633 BB mixture reaches 12 mg C/L, the concentration of photosensitizers in solution can
634 exceed several millimoles. This suggests that the smoke samples in the present study
635 likely contains substantial amounts of photosensitizing compounds. Upon exposure to

636 sunlight, these photosensitizer (denoted as PS) absorb photons and transition to their
 637 triplet excited state ($^3\text{PS}^*$). The excited triplet states can subsequently react with O_2 to
 638 produce various ROS, including $^1\text{O}_2$, superoxide ($\text{O}_2^{\bullet-}$), hydroperoxyl radical ($\bullet\text{HO}_2$),
 639 and $\bullet\text{OH}$, through H-abstrating, electron transfer and energy transfer processes. These
 640 ROS species actively participate in subsequent photooxidation reactions.



652 According to method described in Section 2.7, the steady-state concentrations of $\bullet\text{OH}$
 653 (denoted as $[\bullet\text{OH}]_{\text{ss}}$) and $[^1\text{O}_2]$ (denoted as $[^1\text{O}_2]_{\text{ss}}$) were determined using EPR. The
 654 distinct 1:1:1 triplet EPR signal characteristic of $^1\text{O}_2$ and 1:2:2:1 quartet signal of $\bullet\text{OH}$
 655 confirmed the generation of $^1\text{O}_2$ and $\bullet\text{OH}$, with signal intensities increasing as the
 656 reaction time progressed (Fig. S10). It should be noted that EPR-based spin-trapping
 657 methods have inherent limitations. For example, spectral overlap and background

658 signals may affect the resolution and accuracy of peak assignment. Furthermore, certain
659 short-lived or low-reactivity ROS may not be effectively captured by the selected spin
660 traps. Therefore, the reported ROS contributions should be interpreted as semi-
661 quantitative estimates rather than absolute concentrations

662 Then, a chemical probe method was employed to further quantify the
663 concentrations of $\cdot\text{OH}$ and $^1\text{O}_2$. Benzoic acid (BA) was used as the $\cdot\text{OH}$ probe
664 compound according to previously established protocol (Hu et al., 2025). Briefly, six
665 different concentration of BA (5, 10, 15, 20, 30, 40 and 50 μM) were added to separate
666 aliquots of the same extract. After illuminating for time t , the residual BA concentration
667 was monitored by UPLC-PDA. A linear regression of $-\ln[\text{BA}]/\ln[\text{BA}]_0$ versus reaction
668 time t yielded the pseudo-first-order rate constant (k_{BA}) (Fig. 10 a, b). By plotting the
669 reciprocal ($1/k_{\text{BA}}$) against $[\text{BA}]$, the intercept was obtained (Fig. 10 c), from which
670 $[\text{OH}]_{\text{ss}}$, was determined by dividing the intercept by the second-order rate constants k_{BA} ,
671 OH (Lei et al., 2023). The $k_{\text{BA, OH}}$ is strongly dependent on pH value. Under low pH
672 conditions, benzoic acid predominantly exists in its molecular form (BA), whereas at
673 high pH it is mainly present as the deprotonated species (benzoate, BA^-). These
674 different forms exhibit distinct reactivity toward $\cdot\text{OH}$. According to the literature
675 (Arakaki et al., 2013), when $\text{pH} > 6$, BA^- is the dominant species, with a rate constant
676 $k_{\text{BA}^-, \text{OH}} = 6.0 \times 10^9 \text{ M}^{-1} \text{ s}^{-1}$; when $\text{pH} < 4$, the molecular form dominates, with $k_{\text{BAOH}} = 1.8$
677 $\times 10^9 \text{ M}^{-1} \text{ s}^{-1}$. In this study, the initial pH values of coal and maize samples were 6.79
678 and 5.83, therefore, $5.1 \times 10^9 \text{ M}^{-1} \text{ s}^{-1}$ (Lei et al., 2023) was adopted to calculate the
679 steady-state concentration of OH. The estimated $[\text{OH}]_{\text{ss}}$ were $9.11 \times 10^{-14} \text{ M}$ and
680 $8.58 \times 10^{-14} \text{ M}$ for coal and maize smoke extracts, respectively (Fig. 10)–values

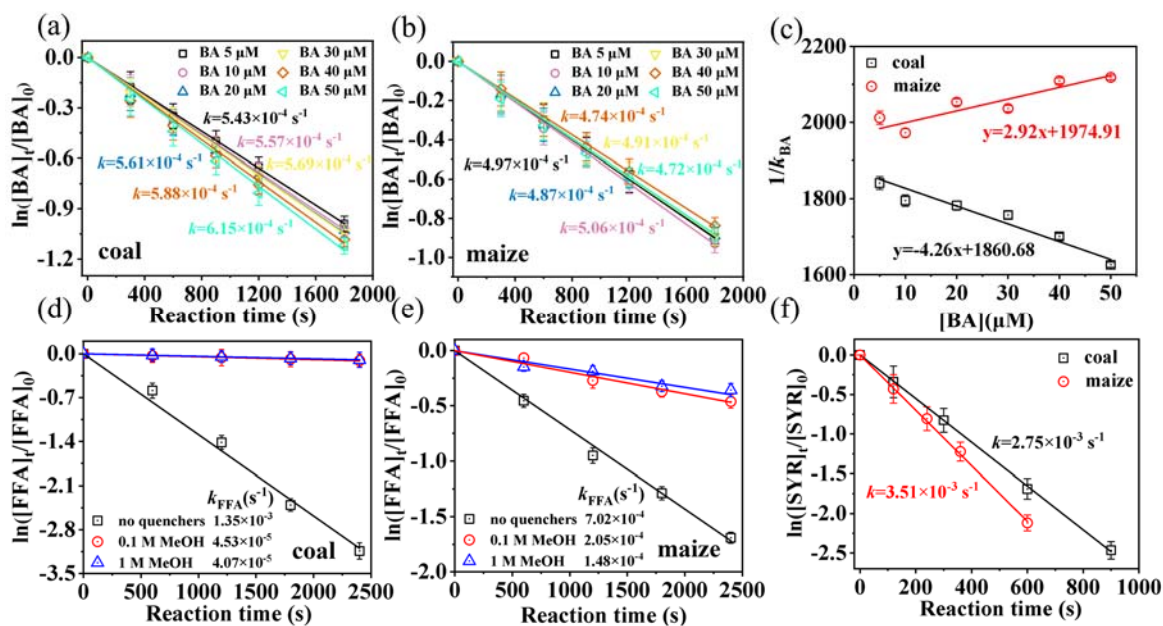
681 comparable to those typically observed in atmospheric cloud droplets (Arakaki et al.,
682 2013; Li et al., 2023).

683 The steady-state concentrations of $^1\text{O}_2$ and $^3\text{C}^*$ were also quantified by monitoring
684 the decay of furfuryl alcohol (FFA) and syringol (SYR) under pseudo-first-order
685 kinetics (Fig. 10 d-f), following previously established procedures (Li et al., 2024).
686 Considering the relatively high $\bullet\text{OH}$ concentration in the mixed system, potential
687 interference may occur when using FFA as a probe, since it can react with both $\bullet\text{OH}$
688 ($k_{\text{FFA}, \text{OH}}=1.5\times 10^{10} \text{ M}^{-1} \text{ s}^{-1}$) and $^1\text{O}_2$ ($k_{\text{FFA}, ^1\text{O}_2}=1.2\times 10^8 \text{ M}^{-1} \text{ s}^{-1}$). To eliminate this
689 interference, excess methanol was added to completely quench $\bullet\text{OH}$ ($k_{\text{MeOH}, \text{OH}}=1.0\times 10^9$
690 $\text{M}^{-1} \text{ s}^{-1}$) before employing FFA to determine the $^1\text{O}_2$ concentration. The results (Fig. 10)
691 showed that the $[^1\text{O}_2]_{\text{ss}}$ values were $3.48\times 10^{-13} \text{ M}$ and $1.8\times 10^{-12} \text{ M}$ for coal and maize
692 smoke extracts, respectively, higher than that reported for 5 mgC L^{-1} of SOA extracts
693 ($3\times 10^{-14} \text{ M}$) (Manfrin et al., 2019). Generally, $^1\text{O}_2$ was born by triplets thus tightly
694 linked to $^3\text{C}^*$. The significantly higher $^1\text{O}_2$ concentration observed in maize smoke
695 extracts—approximately six times that of coal smoke extracts—indicates a greater
696 abundance of triplet-state precursors in maize-derived WSOM. Similarly, SYR was
697 employed as a chemical probe due to its high reactivity with triplets ($k_{\text{SYR}, ^3\text{C}^*}=3.9\times 10^9$
698 $\text{M}^{-1} \text{ s}^{-1}$) (Ma et al., 2023). Based on its pseudo-first-order decay kinetics, the steady-
699 state concentrations of $^3\text{C}^*$ in the maize and coal systems were determined to be
700 $9.0\times 10^{-13} \text{ M}$ and $7.05\times 10^{-13} \text{ M}$, respectively (Fig. 11f).

701 The steady-state concentrations determined in our system are approximately one
702 order of magnitude higher than those reported in aqueous PM extracts illuminated with

703 365 nm lamps (e.g., $\sim 10^{-13}$ M for triplets) (Bogler et al., 2022). Data from Ma et al.
704 (2024) also showed the concentrations of $\bullet\text{OH}$, $^1\text{O}_2$, and $^3\text{C}^*$ in $\text{PM}_{2.5}$ extracts range
705 from $(0.2\text{--}4.7) \times 10^{-15}$ M, $(0.7\text{--}45) \times 10^{-13}$ M, and $(0.03\text{--}7.9) \times 10^{-13}$ M, respectively.
706 This significant difference is mainly attributed to the addition of 10 mM H_2O_2 in our
707 experiments. Given an estimated average molecular weight of 300 g/mol for WSOM,
708 the resulting molar ratio of H_2O_2 to WSOM (15 mg C/L) is approximately 200:1. This
709 substantial excess of H_2O_2 provides a high concentration of $\bullet\text{OH}$, sufficient to
710 extensively oxidize WSOM and explaining why our $\bullet\text{OH}$ levels are orders of magnitude
711 greater than those in typical PM extracts (Ma et al., 2024).

712 Consequently, the degradation of WSOM in our system is predominantly driven
713 by $\bullet\text{OH}$ oxidation, with minor contributions from other reactive species. Furthermore,
714 the concentrations of $^1\text{O}_2$ and $^3\text{C}^*$ were also slightly higher than those in ambient PM
715 extracts (Ma et al., 2024), likely because our simulated combustion samples contained
716 higher levels of phenolic compounds and PAHs, which are known precursors for these
717 species.



718

719 **Fig. 10.** Loss of (a,b) BA, (d,e) FFA, (f) SYR and (c) plot of $1/k_{BA}$ and BA concentration

720 To elucidate the reaction mechanism, the role of different ROS in the photodecay and
 721 light absorbance of smoke extracts were examined. The absorption spectra of smoke
 722 extracts with and without 0.1 M methanol ($\cdot\text{OH}$ quencher) were compared (Fig. S11).
 723 A molar ratio of 2000:1(MeOH: WSOM) was employed, assuming an average
 724 molecular weight of 300 g/mol, to ensure complete scavenging OH given the
 725 comparable second-order rate constants of MeOH and WSOM with $\cdot\text{OH}$ (Liu-Kang et
 726 al., 2024). As shown in Fig. S11, absorbance decay rate decreased markedly, especially
 727 within the first hour, indicating that $\cdot\text{OH}$ play a dominant role in the photodacay of the
 728 extracts.

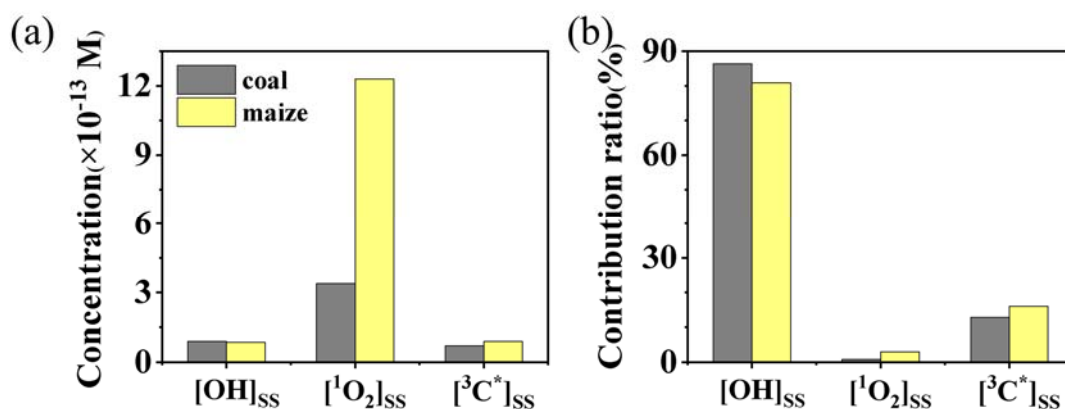
729 To further assess the contributions of individual ROS, comparative experiments
 730 were conducted under N_2 -, air-, and O_2 -saturated conditions. Under N_2 saturation,
 731 secondary oxidants such as $\text{HO}_2\cdot$ and $\cdot\text{OH}$ were largely excluded due to the absence
 732 of oxygen. The changes in WSOC indicate that direct photolysis in both smoke extracts

733 was much weaker than $\bullet\text{OH}$ oxidation. Under $\bullet\text{OH}$ oxidation, the WSOC loss under
734 N_2 -saturated conditions was much lower than that under O_2 - and air-saturated
735 conditions (Fig. S12), whereas in direct photolysis, the differences among the three gas
736 conditions were negligible (Fig. S13). This suggests that O_2 plays a crucial role only
737 for $\bullet\text{OH}$ oxidation.

738 Previous studies have reported that $^3\text{C}^*$ -initiated photooxidation of phenolic
739 compounds proceeds most rapidly under N_2 -saturated conditions (Lei et al., 2023). In
740 contrast, our results showed the fastest degradation under O_2 -saturated and the slowest
741 under N_2 , implying that $^3\text{C}^*$ is not the dominant oxidant in our system. This conclusion
742 is further supported by the comparable WSOC degradation observed for coal and maize
743 smoke extracts. Theoretically, if $^3\text{C}^*$ were the primary oxidant, maize extracts would be
744 expected to exhibit a much higher WSOC degradation owing to their greater content of
745 photosensitizers, as indicated by the higher lignin-like compounds in maize (Section
746 3.3).

747 The relative importance of individual ROS in WSOM photodecay was evaluated
748 by multiplying their corresponding second-order rate constants with their steady-state
749 concentrations. Thus, we estimated the relative role in smoke WSOM photodecay.
750 Given that reaction rates of WSOC with $\bullet\text{OH}$ and $^3\text{C}^*$ were $3.8 \times 10^8 \text{ M}^{-1}\text{s}^{-1}$ and 7.2×10^7
751 $\text{M}^{-1}\text{s}^{-1}$, whereas $^1\text{O}_2$ reacts much more slowly ($10^5 \text{ M}^{-1}\text{s}^{-1}$) (Ma et al., 2024), the
752 contributions were calculated (Fig. 10b). For coal smoke extract, $\bullet\text{OH}$, $^3\text{C}^*$, $^1\text{O}_2$
753 accounted for approximate 86.4%, 12.8% and 0.8% of the total oxidation, respectively.
754 A similar pattern was observed for maize smoke extracts (80.9%, 16.0% and 3.1%),

755 with the overall contribution order of $\cdot\text{OH} > {}^3\text{C}^* > {}^1\text{O}_2$. Although ${}^1\text{O}_2$ exhibited the
 756 highest steady-state concentration, its low reactivity limited its overall contribution,
 757 consistent with previous findings (Zhang et al., 2024). According to earlier reports
 758 (Tang et al., 2025), when the concentration of the BB-derived mixture reaches 12 mg
 759 C/L, the concentration of photosensitizers in solution can exceed several millimoles.
 760 Therefore, ${}^3\text{C}^*$ also plays an important and non-negligible role in the photodegradation
 761 of both smoke WSOM.



762

763 **Fig. 11.** ROS steady-state contribution and their contribution to WSOM photodecay

764 Surely, different H_2O_2 concentrations might influence the relative role of ROS. To
 765 assess this effect, we examined the ROS concentrations and their contributions under
 766 five different H_2O_2 levels (0.5, 1, 3, 5, and 10 mM). The results are presented in Table
 767 S5. As shown in Table S5, increasing the H_2O_2 dosage leads to higher $\cdot\text{OH}$
 768 concentrations and relative contributions, accompanied by a corresponding decrease in
 769 the contribution of triplet excited states (${}^3\text{C}^*$). The measured $\cdot\text{OH}$ concentrations
 770 generally fall within a relatively narrow range under five different H_2O_2 concentration,
 771 with average values of $(0.7 - 9.1) \times 10^{-14}$ M and $(1.3 - 8.3) \times 10^{-14}$ M, for coal and maize
 772 smoke WSOM, respectively. Specifically, we also noted that the ${}^1\text{O}_2$ contribution is only

773 weakly affected by the H₂O₂ concentration. Given that this study mainly focuses on the
774 role of •OH, all subsequent experiments were conducted at a relatively high H₂O₂
775 concentration. While additional experiments at varying H₂O₂ concentrations would
776 provide valuable quantitative constraints on these processes, they are beyond the scope
777 of the present study.

778 **3.6.2 Photochemical transformation of smoke extracts**

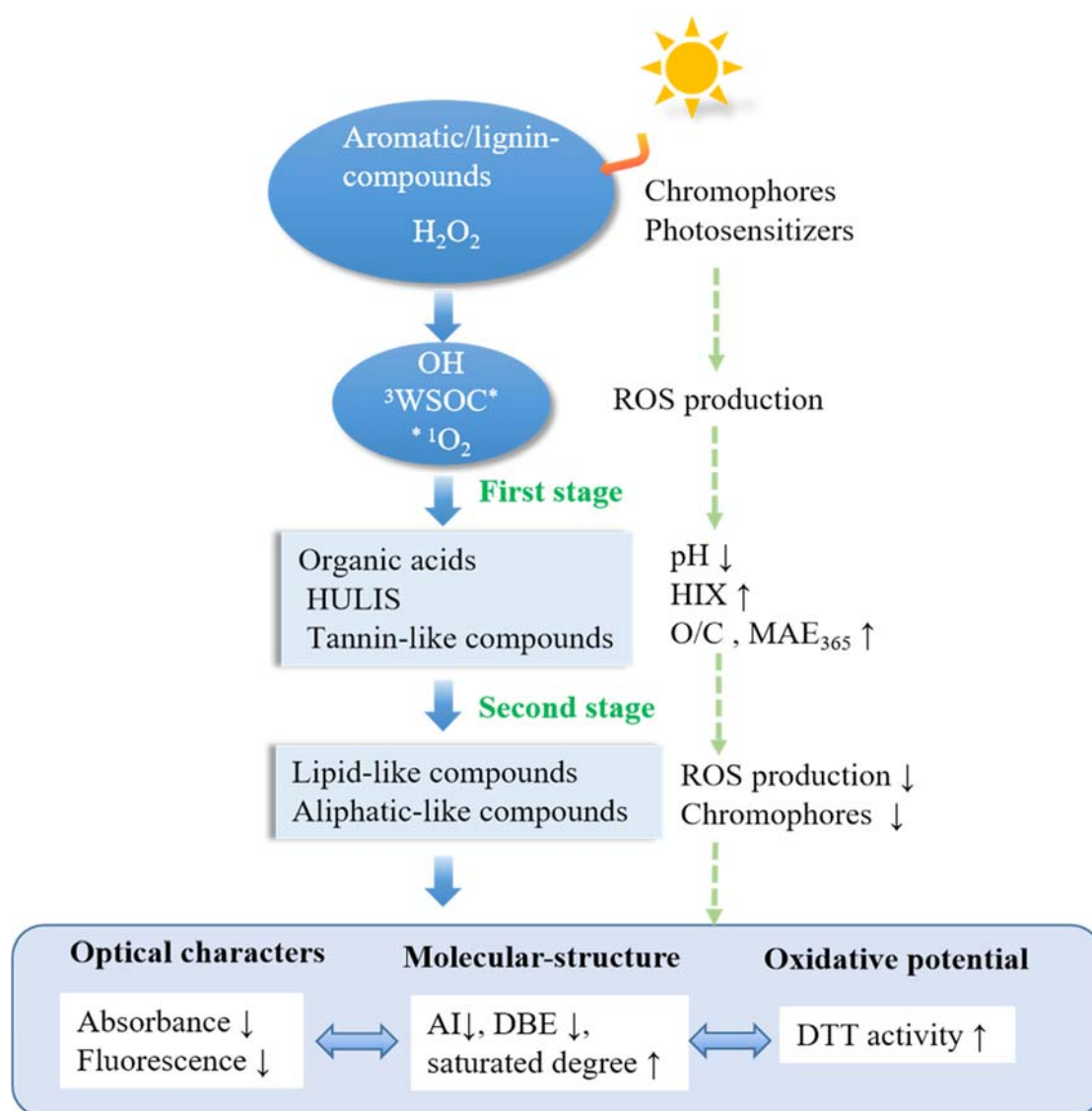
779 By introducing extra H₂O₂, the •OH concentration and its role in the photoaging
780 of both smoke extracts were altered. The added •OH accounts for a major fraction of
781 the total oxidants in both systems, thereby influencing the overall optical properties and
782 chemical composition. Based on the ROS measurements and molecular analyses, a
783 conceptual mechanism for the aqueous photooxidation of both smoke extracts is
784 proposed (Fig. 12). Upon irradiation, photosensitizers in WSOM absorb photons and
785 form triplet excited states (³PS*), which transfer energy or electrons to dissolved O₂,
786 generating various ROS (¹O₂, O₂^{•-}, •HO₂, and •OH). These reactive species initiate and
787 propagate oxidation processes, thereby modifying the chemical composition and optical
788 properties of WSOM.

789 In the first stage, abundant •OH rapidly attacks electron-rich aromatic and
790 conjugated structures, cleaving C=C and C–O bonds and causing a sharp decrease in
791 WSOC and light absorbance. Meanwhile, both ³Sen* and ¹O₂ selectively oxidizes
792 lignin-like compounds, forming oxygenated intermediates such as carbonyls, and
793 carboxylic acids, resulting in gradual decrease in solution pH (Fig. S7) and increase in
794 O/C.

795 As the reaction proceeds, the depletion of aromatic chromophores suppresses
796 further ROS formation, consistent with the observed decline in DTT activity. FT-ICR
797 MS analysis further supports this evolution, revealing a shift from high H/C, low O/C
798 aromatic compounds toward lipid- or aliphatic-like species.

799 Interestingly, although total WSOC decreased with aging, WSOC-normalized
800 DTT activity increased due to probable highly DTT active species (e.g., quinone-like
801 species). Similar trends have been observed in BBOA-WSOC OH-photooxidation
802 aging, where oxidative potential decreased at the initial period (~ 5 h) despite WSOC
803 mass loss (Wong et al., 2019).

804 Overall, the aqueous photooxidation of two smoke extracts involves a dynamic
805 interplay among $\bullet\text{OH}$, $^3\text{C}^*$, and $^1\text{O}_2$. The early stage is dominated by $\bullet\text{OH}$ -driven
806 degradation of chromophores, followed by secondary formation of oxygenated,
807 potentially more toxic species through $^1\text{O}_2$ and triplet-state reactions. These processes
808 jointly govern the chemical evolution, light-absorbing behavior, and oxidative potential
809 of WSOM during photochemical aging.



810
811 **Fig. 12.** Proposed photochemical transformation pathways for two smoke extracts

812 Next, by integrating FT-ICR MS and ROS analyses, we further compared the
813 molecular transformation mechanisms of the two types of smoke. Table S6 and S7 list
814 the top 10 most abundant compounds identified by FT-ICR MS before photolysis and
815 after 11 h and 23 h of irradiation, together with their DBE values, molecular formulas,
816 inferred functional groups, and FT-ICR MS classifications.

817 Fresh coal-derived WSOM is mainly composed of CHO and CHOS compounds,
818 including organosulfates (e.g., C₁₂H₂₆O₄S, C₁₇H₂₈O₃S, and C₁₈H₃₀O₃S), aromatic
819 oxygenated species (e.g., C₁₂H₁₂O₅ and C₁₃H₁₄O₅), and aliphatic compounds (e.g.,
820 C₁₈H₃₆O₃). During photochemical processing, only limited transformation is observed

821 among the top 10 compounds, although partial conversion of lignin-like structures into
822 lipid-like species occurs. Several molecular formulas (e.g., $C_{17}H_{28}O_3S$, $C_{18}H_{30}O_3S$,
823 $C_{16}H_{32}O_2$, and $C_{18}H_{36}O_3$) persist before and after 11 h of irradiation, indicating their
824 relative resistance to photochemical degradation. Consequently, the average molecular
825 weight of coal-derived WSOM exhibits only minor variation during oxidation.

826 The transformation of coal smoke WSOM can be summarized by three main
827 pathways. First, aromatic compounds (e.g., $C_{12}H_{12}O_5$ and $C_{13}H_{14}O_5$) undergo $\cdot OH$ -
828 driven oxidation and tend to break down into smaller molecules, contributing to the loss
829 of aromatic structures. Second, aliphatic compounds (e.g., $C_{18}H_{36}O_3$) are oxidized
830 via $\cdot OH$ -initiated functionalization, forming more stable oxygenated fatty acid-like
831 products such as $C_{16}H_{32}O_2$ and $C_{18}H_{36}O_2$, along with partially oxidized intermediates
832 (e.g., $C_{18}H_{34}O_3$). Third, CHOS compounds exhibit partial stability, with long-chain
833 organosulfates (e.g., $C_{18}H_{30}O_3S$) persisting throughout the oxidation process.

834 In contrast, maize smoke WSOM shows distinctly different behavior. The fresh
835 sample was dominated by lignin-like compounds, such as $C_9H_{10}O_3$ and $C_9H_8O_3$,
836 reflecting the prevalence of aromatic structures derived from biomass combustion.
837 During aqueous-phase oxidation, these compounds undergo extensive transformation
838 driven primarily by $\cdot OH$ attack, including hydrogen abstraction and electrophilic
839 addition to aromatic rings. These reactions promote hydroxylation, denitration, and
840 subsequent ring-opening processes, leading to the formation of highly oxygenated and
841 lower-molecular-weight products. As a result, both aromaticity and average molecular
842 weight decrease significantly. This trend is supported by the appearance of highly
843 oxygenated species (e.g., $C_9H_{10}O_7$ and $C_9H_{18}O_6$ at 11 h), which shift toward higher O/C
844 ratios in the Van Krevelen space. Meanwhile, lignin-like compounds are progressively
845 transformed into lipid-like, tannin-like, and aliphatic species. Notably, the top 10

846 products at 11 h and 23 h exhibit strong similarity (e.g., C₁₄H₂₂O, C₁₆H₃₂O₂, C₁₈H₃₆O₂,
847 and C₁₂H₂₆O₄S), suggesting the formation of relatively stable oxidation products at later
848 stages.

849 Overall, these results demonstrate that maize smoke undergoes more extensive
850 oxidation, characterized by pronounced aromatic degradation and molecular
851 fragmentation, whereas coal smoke exhibits higher chemical stability, with limited
852 molecular transformation and a greater persistence of initial compounds.

853 **4 Conclusions**

854 This study systematically investigated the aqueous-phase •OH-driven
855 photodegradation of coal and maize smoke extracts, providing molecular-level insights
856 into their molecular and optical evolution. EEM-PARAFAC resolved one humic-like
857 and two protein-like components, revealing distinct temporal patterns between coal and
858 maize systems. FT-ICR MS further showed that both samples were dominated by CHO
859 and CHON compounds, with maize smoke enriched in CHON species and coal smoke
860 containing a higher fraction of sulfur-containing compounds.

861 Aqueous photooxidation led to increased molecular saturation and reduced
862 aromaticity, as evidenced by declining DBE and AI values. Lignin-like compounds
863 were progressively depleted, accompanied by an increase in lipid- and aliphatic-like
864 species, suggesting the breakdown of conjugated structures and the formation of more
865 saturated, oxygenated products. These transformations reduced chromophoric content
866 through double-bond cleavage and aromatic ring opening, resulting in decreased light
867 absorption and fluorescence.

868 The contributions of ROS to photodegradation followed the order •OH > ³C* >
869 ¹O₂, highlighting the dominant role of •OH in aqueous-phase processing. Despite these
870 common trends, distinct photochemical pathways were observed. Maize-derived

871 WSOM exhibited more rapid oxidation during the early stage, likely driven by OH-
872 functionalization reactions, whereas coal-derived WSOM showed greater
873 compositional stability. Mechanistically, ROS promoted the conversion of lignin-like
874 aromatics into highly oxygenated products via hydroxylation and ring-opening, while
875 lipid-like compounds undergo functionalization and fragmentation. Secondary
876 reactions with sulfate lead to the formation of organosulfates.

877 HR-AMS results confirmed the formation of low-molecular-weight carboxylic
878 acids (e.g., oxalate), accompanied by decreasing pH and increasing oxidation state of
879 aqSOA, particularly in maize systems. Although total WSOC decreased during
880 photodegradation, the WSOC-normalized oxidative potential increased, as indicated by
881 enhanced DTT consumption, likely due to the formation of nitrogen-containing
882 compounds in coal smoke and reactive quinones in maize smoke. Furthermore, maize-
883 derived aqSOA exhibited higher oxidation levels, whereas coal smoke produced higher
884 aqSOA mass yields.

885 Overall, aqueous-phase photochemical processing simultaneously weakens
886 optical properties and enhances chemical reactivity. From an atmospheric perspective,
887 cloud and fog processing can substantially modify the properties of smoke-derived
888 WSOM. The transformation of aromatic chromophores into more saturated products
889 reduces brown carbon light absorption, potentially weakening its direct radiative
890 forcing. At the same time, the formation of highly oxidized and redox-active species
891 may enhance aerosol oxidative potential and toxicity. These findings underscore the
892 importance of incorporating aqueous-phase transformations into atmospheric models
893 to more accurately assess the climate and air quality impacts of emissions from different
894 fuel sources.

895 **Author contributions.**

896 ZY and XG developed the research objectives and designed the experiments. DH
897 and XH set up the combustion sampling apparatus and collected samples. DH and QC
898 conducted the photochemistry experiments and analyzed the data with the help of XH.
899 ZY prepared the manuscript with contributions from all co-authors. ZY and XG
900 provided supervision and guidance during the experiments and writing.

901 **Acknowledgements.**

902 The authors acknowledge support from the Natural Science Foundation of Jiangsu
903 Province (BK20221405) and National foreign expert project (H20240368). We are also
904 thankful for funding support from Natural Science Foundation of China (22361162668),
905 Natural Science Foundation of the Jiangsu Higher Education Institutions of China
906 (25KJD170010), and the Postgraduate Research & Practice Innovation Program of
907 Jiangsu Province (SJCX24_1808).

908 **References**

- 909 Arakaki, T., Anastasio, C., Kuroki, Y., Nakajima, H., Okada, K., Kotani, Y., Handa, D., Azechi, S.,
910 Kimura, T., Tsuchioka, A., and Miyagi, Y.: A general scavenging rate constant for reaction of
911 hydroxyl radical with organic carbon in atmospheric waters, *Environ. Sci. Technol.*, 47, 8196–
912 8203, <https://doi.org/10.1021/es401927b>, 2013.
- 913 Arciva, S., Niedek, C., Mavis, C., Yoon, M., Sanchez, M. E., Zhang, Q., and Anastasio, C.:
914 Aqueous ·OH oxidation of highly substituted phenols as a source of secondary organic aerosol,
915 *Environ. Sci. Technol.*, 56, 9959–9967, <https://doi.org/10.1021/acs.est.2c02225>, 2022.
- 916 Arciva, S., Ma, L., Mavis, C., Guzman, C., and Anastasio, C.: Formation and loss of light
917 absorbance by phenolic aqueous SOA by OH and an organic triplet excited state, *Atmos. Chem.*
918 *Phys.*, 24, 4473–4485, <https://doi.org/10.5194/acp-24-4473-2024>, 2024.
- 919 Bogler, S., Daellenbach, K. R., Bell, D. M., Prévôt, A. S. H., El Haddad, I., and Borduas-Dedekind,
920 N.: Singlet oxygen seasonality in aqueous PM₁₀ is driven by biomass burning and anthropogenic
921 secondary organic aerosol, *Environ. Sci. Technol.*, 56, 15389–15397,
922 <https://doi.org/10.1021/acs.est.2c04554>, 2022.
- 923 Cao, T., Xu, C., Chen, H., Song, J., Li, J., Song, H., Jiang, B., Zhong, Y., and Peng, P.: Molecular
924 insight into aqueous-phase photolysis and photooxidation of water-soluble organic matter emitted

925 from biomass burning and coal combustion, *Atmos. Chem. Phys.*, 25, 11597–11610,
926 <https://doi.org/10.5194/acp-25-11597-2025>, 2025.

927 Chen, Q., Wang, M., Wang, Y., Zhang, L., Li, Y., and Han, Y.: Oxidative potential of water-soluble
928 matter associated with chromophoric substances in PM_{2.5} over Xi'an, China, *Environ. Sci.*
929 *Technol.*, 53, 8574–8584, <https://doi.org/10.1021/acs.est.9b01976>, 2019.

930 Chen, W., Zhang, H., Xu, S., Jia, H., Qi, Z., Farooq, U., Wang, Z., and Dai, Q.: New insights into
931 the molecular characteristics-dependent light absorption variation of water-soluble organic matter
932 in biomass burning smoke, *Atmos. Res.*, 316, 107951,
933 <https://doi.org/10.1016/j.atmosres.2025.107951>, 2025.

934 Cook, R. D., Lin, Y.-H., Peng, Z., Boone, E., Chu, R. K., Dukett, J. E., Gunsch, M. J., Zhang, W.,
935 Tolic, N., Laskin, A., and Pratt, K. A.: Biogenic, urban, and wildfire influences on the molecular
936 composition of dissolved organic compounds in cloud water, *Atmos. Chem. Phys.*, 17, 15167–
937 15180, <https://doi.org/10.5194/acp-17-15167-2017>, 2017.

938 Fan, X., Wei, S., Zhu, M., Song, J., and Peng, P.: Comprehensive characterization of humic-like
939 substances in smoke PM_{2.5} emitted from the combustion of biomass materials and fossil fuels,
940 *Atmos. Chem. Phys.*, 16, 13321–13340, <https://doi.org/10.5194/acp-16-13321-2016>, 2016.

941 Fan, X., Li, M., Cao, T., Cheng, C., Li, F., Xie, Y., Wei, S., Song, J., and Peng, P.: Optical properties
942 and oxidative potential of water- and alkaline-soluble brown carbon in smoke particles emitted
943 from laboratory simulated biomass burning, *Atmos. Environ.*, 194, 48–57,
944 <https://doi.org/10.1016/j.atmosenv.2018.09.025>, 2018.

945 Fan, X., Xie, S., Yu, X., Cheng, A., Chen, D., Ji, W., Liu, X., Song, J., and Peng, P.: Molecular-
946 level transformations of biomass burning-derived water-soluble organic carbon during dark
947 aqueous OH oxidation: Insights from absorption, fluorescence, high-performance size exclusion
948 chromatography and high-resolution mass spectrometry analysis, *Sci. Total Environ.*, 912,
949 169290, <https://doi.org/10.1016/j.scitotenv.2023.169290>, 2024.

950 Fang, Z., Lai, A., Cai, D., Li, C., Carmieli, R., Chen, J., Wang, X., and Rudich, Y.: Secondary
951 organic aerosol generated from biomass burning emitted phenolic compounds: Oxidative
952 potential, reactive oxygen species, and cytotoxicity, *Environ. Sci. Technol.*, 58, 8194–8206,
953 <https://doi.org/10.1021/acs.est.3c09903>, 2024.

954 Gerritz, L., Wei, J., Fang, T., Wong, C., Klodt, A. L., Nizkorodov, S. A., and Shiraiwa, M.: Reactive
955 oxygen species formation and peroxide and carbonyl decomposition in aqueous photolysis of
956 secondary organic aerosols, *Environ. Sci. Technol.*, 58, 4716–4726,
957 <https://doi.org/10.1021/acs.est.3c08662>, 2024.

958 Go, B. R., Li, Y. J., Huang, D. D., Wang, Y., and Chan, C. K.: Comparison of aqueous secondary
959 organic aerosol (aqSOA) product distributions from guaiacol oxidation by non-phenolic and
960 phenolic methoxybenzaldehydes as photosensitizers in the absence and presence of ammonium
961 nitrate, *Atmos. Chem. Phys.*, 23, 2859–2875, <https://doi.org/10.5194/acp-23-2859-2023>, 2023.

962 Go, B. R., Li, Y. J., Huang, D. D., and Chan, C. K.: Aqueous-phase photoreactions of mixed
963 aromatic carbonyl photosensitizers yield more oxygenated, oxidized, and less light-absorbing
964 secondary organic aerosol (SOA) than single systems, *Environ. Sci. Technol.*, 58, 7924–7936,
965 <https://doi.org/10.1021/acs.est.3c10199>, 2024.

966 Hems, R. F., Schnitzler, E. G., Bastawrous, M., Soong, R., Simpson, A. J., and Abbatt, J. P. D.:
967 Aqueous photoreactions of wood smoke brown carbon, *ACS Earth Space Chem.*, 4, 1149–1160,
968 <https://doi.org/10.1021/acsearthspacechem.0c00117>, 2020.

969 Hu, D., Ye, Z., Wang, Z., Topping, D., Aruffo, E., Wang, H., and Ge, X.: Kinetics and quantum
970 yield of photosensitized reactions from substituted phenols via chemical probe approach, *Atmos.*
971 *Environ.*, 360, 121419, <https://doi.org/10.1016/j.atmosenv.2025.121419>, 2025a.

972 Hu, D., Wang, Z., Aruffo, E., Dai, X., Zhao, Z., and Ye, Z.: Kinetics of different substituted Phenolic
973 compounds' aqueous OH oxidation in atmosphere, *Atmosphere*, 16,
974 <https://doi.org/10.3390/atmos16050567>, 2025b.

975 Huang, Y., Li, X., Huang, D. D., Lei, R., Zhou, B., Zhang, Y., and Ge, X.: Machine-learning-
976 assisted chemical characterization and optical properties of atmospheric brown carbon in Nanjing,
977 China, *Atmos. Chem. Phys.*, 25, 7619–7645, <https://doi.org/10.5194/acp-25-7619-2025>, 2025.

978 Jiang, H. and Jang, M.: Dynamic oxidative potential of atmospheric organic aerosol under ambient
979 sunlight, *Environ. Sci. Technol.*, 52, 7496–7504, <https://doi.org/10.1021/acs.est.8b00148>, 2018.

980 Jiang, W., Misovich, M. V., Hettiyadura, A. P. S., Laskin, A., McFall, A. S., Anastasio, C., and
981 Zhang, Q.: Photosensitized reactions of a phenolic carbonyl from wood combustion in the
982 aqueous phase—Chemical evolution and light absorption properties of aqSOA, *Environ. Sci.*
983 *Technol.*, <https://doi.org/10.1021/acs.est.0c07581>, 2021.

984 Jiang, W., Niedek, C., Anastasio, C., and Zhang, Q.: Photoaging of phenolic secondary organic
985 aerosol in the aqueous phase: evolution of chemical and optical properties and effects of oxidants,
986 *Atmos. Chem. Phys.*, 23, 7103–7120, <https://doi.org/10.5194/acp-23-7103-2023>, 2023.

987 Lei, R., Sha, Y., Meng, H., Huang, Y., Ye, J., Huang, D. D., Zhang, Y., Wu, Y., Li, Y., and Ge, X.:
988 Aqueous phase photolysis of 4-nitrocatechol: Reaction kinetics, evolutions of chemical
989 composition, light absorption and oxidation potential, *Atmos. Environ.*, 343, 120981,
990 <https://doi.org/10.1016/j.atmosenv.2024.120981>, 2025.

991 Lei, Y., Yu, Y., Lei, X., Liang, X., Cheng, S., Ouyang, G., and Yang, X.: Assessing the use of
992 probes and quenchers for understanding the reactive species in advanced oxidation processes,
993 *Environ. Sci. Technol.*, 57, 5433–5444, <https://doi.org/10.1021/acs.est.2c09338>, 2023.

994 Lei, Y., Lei, X., Tian, G., Yang, J., Huang, D., Yang, X., Chen, C., and Zhao, J.: Optical variation
995 and molecular transformation of brown carbon during oxidation by NO₃• in the aqueous phase,
996 *Environ. Sci. Technol.*, 58, 3353–3362, <https://doi.org/10.1021/acs.est.3c08726>, 2024.

- 997 Leresche, F., Salazar, J. R., Pfothner, D. J., Hannigan, M. P., Majestic, B. J., and Rosario-Ortiz,
998 F. L.: Photochemical aging of atmospheric particulate matter in the aqueous phase, *Environ. Sci.*
999 *Technol.*, 55, 13152–13163, <https://doi.org/10.1021/acs.est.1c00978>, 2021.
- 1000 Li, F., Tsona, N. T., Li, J., and Du, L.: Aqueous-phase oxidation of syringic acid emitted from
1001 biomass burning: Formation of light-absorbing compounds, *Sci. Total Environ.*, 765, 144239,
1002 <https://doi.org/10.1016/j.scitotenv.2020.144239>, 2021.
- 1003 Li, F., Zhou, S., Du, L., Zhao, J., Hang, J., and Wang, X.: Aqueous-phase chemistry of atmospheric
1004 phenolic compounds: A critical review of laboratory studies, *Sci. Total Environ.*, 856, 158895,
1005 <https://doi.org/10.1016/j.scitotenv.2022.158895>, 2023.
- 1006 Li, F., Zhou, S., Zhao, J., Hang, J., Lu, H., Li, X., Gao, M., Li, Y., and Wang, X.: Aqueous
1007 photosensitization of syringaldehyde: Reactivity, effects of environmental factors, and formation
1008 of brown carbon products, *ACS Earth Space Chem.*, 8, 1193–1203,
1009 <https://doi.org/10.1021/acsearthspacechem.4c00004>, 2024a.
- 1010 Li, L., Han, Y., Li, J., Lin, Y., Zhang, X., Wang, Q., and Cao, J.: Effects of photochemical aging on
1011 the molecular composition of organic aerosols derived from agricultural biomass burning in
1012 whole combustion process, *Sci. Total Environ.*, 946, 174152,
1013 <https://doi.org/10.1016/j.scitotenv.2024.174152>, 2024b.
- 1014 Lin, P., Aiona, P. K., Li, Y., Shiraiwa, M., Laskin, J., Nizkorodov, S. A., and Laskin, A.: Molecular
1015 characterization of brown carbon in biomass burning aerosol particles, *Environ. Sci. Technol.*, 50,
1016 11815–11824, <https://doi.org/10.1021/acs.est.6b03024>, 2016.
- 1017 Li, X., Tao, Y., Zhu, L., Ma, S., Luo, S., Zhao, Z., Sun, N., Ge, X., and Ye, Z.: Optical and chemical
1018 properties and oxidative potential of aqueous-phase products from OH and $^3\text{C}^{\square}$ -initiated
1019 photooxidation of eugenol, *Atmos. Chem. Phys.*, 22, 7793–7814, [https://doi.org/10.5194/acp-22-](https://doi.org/10.5194/acp-22-7793-2022)
1020 [7793-2022](https://doi.org/10.5194/acp-22-7793-2022), 2022.
- 1021 Liu-Kang, C., Sokolova, A., Gong, Y., Fahy, W. D., Peng, H., and Abbatt, J. P. D.: Light exposure
1022 of wood smoke aerosol: Connecting optical properties, oxidation, radical formation, and chemical
1023 composition, *ACS EST Air*, 1, 273–282, <https://doi.org/10.1021/acsestair.3c00063>, 2024.
- 1024 Ma, L., Worland, R., Jiang, W., Niedek, C., Guzman, C., Bein, K. J., Zhang, Q., and Anastasio, C.:
1025 Predicting photooxidant concentrations in aerosol liquid water based on laboratory extracts of
1026 ambient particles, *Atmos. Chem. Phys.*, 23, 8805–8821, [https://doi.org/10.5194/acp-23-8805-](https://doi.org/10.5194/acp-23-8805-2023)
1027 [2023](https://doi.org/10.5194/acp-23-8805-2023), 2023.
- 1028 Ma, L., Worland, R., Heinlein, L., Guzman, C., Jiang, W., Niedek, C., Bein, K. J., Zhang, Q., and
1029 Anastasio, C.: Seasonal variations in photooxidant formation and light absorption in aqueous
1030 extracts of ambient particles, *Atmos. Chem. Phys.*, 24, 1–21, [https://doi.org/10.5194/acp-24-1-](https://doi.org/10.5194/acp-24-1-2024)
1031 [2024](https://doi.org/10.5194/acp-24-1-2024), 2024.
- 1032 Mahamuni, G., Rutherford, J., Davis, J., Molnar, E., Posner, J. D., Seto, E., Korshin, G., and
1033 Novosselov, I.: Excitation–emission matrix spectroscopy for analysis of chemical composition of

1034 combustion generated particulate matter, *Environ. Sci. Technol.*, 54, 8198–8209,
1035 <https://doi.org/10.1021/acs.est.0c01110>, 2020.

1036 Manfrin, A., Nizkorodov, S. A., Malecha, K. T., Getzinger, G. J., McNeill, K., and Borduas-
1037 Dedekind, N.: Reactive oxygen species production from secondary organic aerosols: The
1038 importance of singlet oxygen, *Environ. Sci. Technol.*, 53, 8553–8562,
1039 <https://doi.org/10.1021/acs.est.9b01609>, 2019.

1040 Ning, C., Tang, Y., Sun, S., Wang, D., and Gao, Y.: Molecular level characteristics and sources of
1041 rainwater water-soluble organic matter in different regions of China by FT-ICR MS, *Atmos.*
1042 *Environ.*, 350, 121175, <https://doi.org/10.1016/j.atmosenv.2025.121175>, 2025.

1043 Song, J., Li, M., Jiang, B., Wei, S., Fan, X., and Peng, P.: Molecular characterization of water-
1044 soluble humic like substances in smoke particles emitted from combustion of biomass materials
1045 and coal using ultrahigh-resolution electrospray ionization Fourier Transform Ion Cyclotron
1046 Resonance Mass Spectrometry, *Environ. Sci. Technol.*, 52, 2575–2585,
1047 <https://doi.org/10.1021/acs.est.7b06126>, 2018.

1048 Tang, J., Li, J., Su, T., Han, Y., Mo, Y., Jiang, H., Cui, M., Jiang, B., Chen, Y., Tang, J., Song, J.,
1049 Peng, P., and Zhang, G.: Molecular compositions and optical properties of dissolved brown
1050 carbon in biomass burning, coal combustion, and vehicle emission aerosols illuminated by
1051 excitation–emission matrix spectroscopy and Fourier transform ion cyclotron resonance mass
1052 spectrometry analysis, *Atmos. Chem. Phys.*, 20, 2513–2532, [https://doi.org/10.5194/acp-20-](https://doi.org/10.5194/acp-20-2513-2020)
1053 [2513-2020](https://doi.org/10.5194/acp-20-2513-2020), 2020.

1054 Tang, R., Ma, J., Zhang, R., Cui, W., Qin, Y., Chu, Y., Qin, Y., Vogel, A. L., and Chan, C. K.:
1055 Enhanced sulfate formation in mixed biomass burning and sea-salt interactions mediated by
1056 photosensitization: effects of chloride, nitrogen-containing compounds, and atmospheric aging,
1057 *Atmos. Chem. Phys.*, 25, 425–439, <https://doi.org/10.5194/acp-25-425-2025>, 2025.

1058 Tomaz, S., Cui, T., Chen, Y., Sexton, K. G., Roberts, J. M., Warneke, C., Yokelson, R. J., Surratt,
1059 J. D., and Turpin, B. J.: Photochemical cloud processing of primary wildfire emissions as a
1060 potential source of secondary organic aerosol, *Environ. Sci. Technol.*, 52, 11027–11037,
1061 <https://doi.org/10.1021/acs.est.8b03293>, 2018.

1062 Verma, V., Rico-Martinez, R., Kotra, N., King, L., Liu, J., Snell, T. W., and Weber, R. J.:
1063 Contribution of water-soluble and insoluble components and their hydrophobic/hydrophilic
1064 subfractions to the reactive oxygen species-generating potential of fine ambient aerosols, *Environ.*
1065 *Sci. Technol.*, 46, 11384–11392, <https://doi.org/10.1021/es302484r>, 2012.

1066 Vione, D., Albinet, A., Barsotti, F., Mekic, M., Jiang, B., Minero, C., Brigante, M., and Gligorovski,
1067 S.: Formation of substances with humic-like fluorescence properties, upon photoinduced
1068 oligomerization of typical phenolic compounds emitted by biomass burning, *Atmos. Environ.*,
1069 206, 197–207, <https://doi.org/10.1016/j.atmosenv.2019.03.005>, 2019.

1070 Wang, H., Zheng, N., Du, H., Chen, Z., Sha, H., Zhou, H., and Ye, Z.: Microheterogeneous
1071 photogeneration of hydroxyl radical in sunlit dissolved black carbon solution, *J. Hazard. Mater.*,
1072 498, 139840, <https://doi.org/10.1016/j.jhazmat.2025.139840>, 2025.

1073 Wang, J. and Wang, S.: Reactive species in advanced oxidation processes: Formation, identification
1074 and reaction mechanism, *Chem. Eng. J.*, 401, 126158, [https://doi.org/10.1016/j.cej.](https://doi.org/10.1016/j.cej.2020.126158),
1075 2020.1261582020, 2020.

1076 Wang, X., Hayeck, N., Brüggemann, M., Yao, L., Chen, H., Zhang, C., Emmelin, C., Chen, J.,
1077 George, C., and Wang, L.: Chemical characteristics of organic aerosols in Shanghai: A study by
1078 ultrahigh-performance liquid chromatography coupled with orbitrap mass spectrometry, *J.*
1079 *Geophys. Res. Atmos.*, 122, 11,703–11,722, <https://doi.org/10.1002/2017JD026930>, 2017.

1080 Wong, J. P. S., Nenes, A., and Weber, R. J.: Changes in light absorptivity of molecular weight
1081 separated brown carbon due to photolytic aging, *Environ. Sci. Technol.*, 51, 8414–8421,
1082 <https://doi.org/10.1021/acs.est.7b01739>, 2017.

1083 Wong, J. P. S., Tsagkaraki, M., Tsiodra, I., Mihalopoulos, N., Violaki, K., Kanakidou, M., Sciare,
1084 J., Nenes, A., and Weber, R. J.: Effects of atmospheric processing on the oxidative potential of
1085 biomass burning organic aerosols, *Environ. Sci. Technol.*, 53, 6747–6756,
1086 <https://doi.org/10.1021/acs.est.9b01034>, 2019.

1087 Wu, G., Fu, P., Ram, K., Song, J., Chen, Q., Kawamura, K., Wan, X., Kang, S., Wang, X., Laskin,
1088 A., and Cong, Z.: Fluorescence characteristics of water-soluble organic carbon in atmospheric
1089 aerosol, *Environ. Pollut.*, 268, 115906, <https://doi.org/10.1016/j.envpol.2020.115906>, 2021.

1090 Yang, N., Wang, J., Jacob, D. J., Ye, J., Sheng, M., Niu, M., Qin, Y., Ge, X., Sun, Y., Wang, Z.,
1091 Wang, Y., Wu, F., Liu, C.-Q., George, C., and Fu, P.: Aqueous production of sulfur-containing
1092 aerosols from nitroaromatic compounds and SO₂ in wintertime urban haze, *Sci. Bull.*, 70, 1846–
1093 1855, <https://doi.org/10.1016/j.scib.2025.03.013>, 2025.

1094 Ye, Z., Hu, D., Wang, Z., Wang, H., and Ge, X.: Aqueous photochemical aging of water-soluble
1095 smoke particles from crop straws burning, *Atmos. Environ.*, 340, 120897,
1096 <https://doi.org/10.1016/j.atmosenv.2024.120897>, 2025.

1097 Zhang, H., Wu, L., Qian, W., Ni, J., Wei, R., Qi, Z., and Chen, W.: Spectral characteristics of
1098 dissolved organic carbon derived from biomass-pyrogenic smoke (SDOC) in the aqueous
1099 environment and its solubilization effect on hydrophobic organic pollutants, *Water Res.*, 203,
1100 117515, <https://doi.org/10.1016/j.watres.2021.117515>, 2021.

1101 Zhang, J., Shrivastava, M., Ma, L., Jiang, W., Anastasio, C., Zhang, Q., and Zelenyuk, A.: Modeling
1102 novel aqueous particle and cloud chemistry processes of biomass burning phenols and their
1103 potential to form secondary organic aerosols, *Environ. Sci. Technol.*, 58, 3776–3786,
1104 <https://doi.org/10.1021/acs.est.3c07762>, 2024.

1105